2014-01-30

Alignments of Radio Source in the ELAIS N1 Deep Field

Jagannathan, Preshanth

UNIVERSITY OF CALGARY

Alignments of Radio Sources in the GMRT ELAIS N1 Deep Field

by

Preshanth Jagannathan

A DISSERTATION

SUBMITTED TO THE FACULTY OF GRADUATE STUDIES

IN PARTIAL FULFILLMENT OF THE REQUIREMENTS FOR THE

DEGREE OF MASTER OF SCIENCE

DEPARTMENT OF PHYSICS AND ASTRONOMY

CALGARY, ALBERTA

January, 2014

Abstract

Results of the AGN jets position angle alignments in the ELAIS N1 Deep radio survey are presented here. The ELAIS N1 deep radio survey was carried out with the Giant Meterwave Radio Telescope at 615 MHz. The deep field is a seven pointing mosaic that covers $1.2deg^2$ centred at $\alpha_{2000} = 16^h10^m35^s$ and $\delta_{2000} = 54°35'$ with an average angular resolution of 5" $\times$ 5" across the mosaic. The average sensitivity of the mosaicked image is 10μJy/beam in Stokes I. There were 65 extended radio galaxy jets extracted from the image of which 33 galaxies have redshift information available. The positions angles of radio galaxy jets are expected to be uniform. The radio galaxy jets in our sample were found to deviate from uniform distribution of positions angles to 99 percent significance level. Further testing with angular covariance reveals alignments in radio position angles, across angular scales of 1.2 to 1.8 °. Position angle correlations at scales of 1.2 to 1.8 °translates to a comoving scale of 50-75 h^{-1}Mpc at $z = 1$. These results corroborate prior evidence for large scale alignments in quasar optical polarization derived by Hutsemékers (1998).

Acknowledgements

The completion of this work would not have been possible if not for the help, guidance and encouragement of many people. I would like to thank my supervisor Russ Taylor for widening my horizons and guiding me by example, be it observations or data reduction. Many thanks to Jeroen Stil who has spent many hours answering my questions, and playing devil's advocate. Thanks Christian Smith for keeping the cluster, network and the conversation going. To my wife, Ramya who saw me through the ups and downs at work and at home these past two years, thank you.

I would like to thank Sanjay Bhatnagar and Urvashi Rau for their patient responses to my CASA queries ever since the synthesis imaging workshop. Observations with the GMRT were smooth and painless thanks to the staff on-site. Thanks to Nimisha Kantharia at NCRA who made our primary beam observations possible, which forms an integral part of this work.

Table of Contents

List of Tables

List of Figures and Illustrations

Chapter 1

Introduction

The current background assumption of modern cosmological theories such as ΛCDM is that universe is isotropic on large scales. There have been several observational studies to detect deviations from isotropy in the past. This has particularly been seen with the cosmic microwave background, where the alignment of the quadrupole and octupole point to the violation of isotropy in the background cosmology. Alignments of galaxy position angles in the sky is another way to probe the violation of isotropy and was first devised by Hawley and Peebles (1975). If detected, the presence of alignments and certain preferred orientations can shed light on the origin and evolution of the galaxies. The role of fundamental forces can be gleaned from the alignment data. A cause of the alignment could be the presence of an external field during galaxy formation or evolution. Cosmic magnetic fields have been shown to be present on scales of galaxy clusters and largerRatra (1992). Effects of seed magnetic fields from inflation Ratra (1992), axionic fields post inflation, and cosmic strings complete the possible candidates that can effect an alignment in galaxies even on scalesw larger than galaxy clusters. One approach to the detection of alignments is using the direction of jets of Radio Galaxies.

The radio sky is nearly isotropic(Condon et al. (1998)), so a sensitive survey covering a small area of the sky provides a representative sample volume for study. Such a sensitive survey is the GMRT ELAIS N1 survey which forms the core of this thesis. There are two distinct populations of extra galactic sources; the first comprising of radio galaxies (Matthews and Sandage (1963))and quasars (Seyfert (1943)) are powered by a central black-hole recognizable by their radio jets and the second category consists of normal galaxies where radio emission comes from energy injection from stars and their stellar remnants.

The emission processes for the two populations of objects are also different. The primary emission mechanism in radio galaxies and quasars is synchrotron radiation. Normal galaxies in addition to synchrotron radiation also exhibit Free-Free emission from H II regions. The source of the relativistic electrons in AGN is the central accreting black-hole. Radio galaxies and quasars are powered by an active galactic nucleus (AGN) that is present at the centre of the galaxy and their jets are the most commonly observed sources in a radio survey. AGN are conventionally classified as Radio-loud and Radio-quiet. In radio-loud objects the emission contribution is dominated by the jets and the radio lobes and hence are the primary target of this study, in radio quiet AGN the emission is dominated by the core of the galaxy. A broad unification scheme exists for AGN(Lawrence (1987)) that provides a complete picture and explains that the differences in source orientation as the source for the different classifications of AGN. The unified scheme of AGN is represented pictorially in figure 1.1

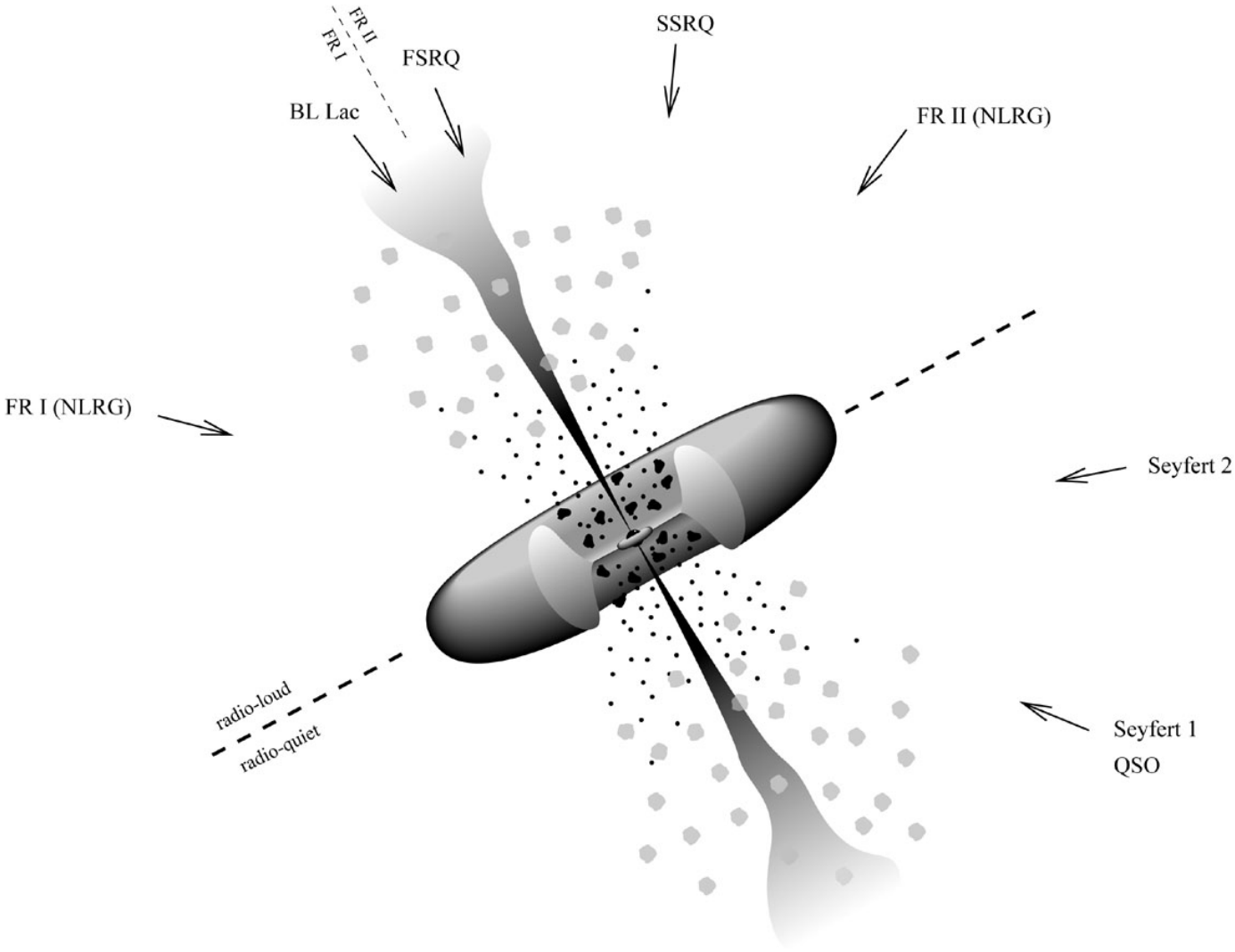

Figure 1.1: The unification model for AGNs from the Torres and Anchordoqui (2004) review. Blazars are those AGNs for which the jets are close to line of sight. A regular quasar or a Seyfert 1 galaxy is observed if the orientation angle is 30°, where the narrow-line and broad-line regions are visible. At larger angular offsets, the broad-line region will be hidden by the torus, the corresponding class being Seyfert 2 galaxies. Perpendicular to the jet axis, the full extent of the jets may be seen particularly at low frequencies, giving rise to a morphology typical of radio galaxies.

1.0.1 Active Galactic Nucleus and Relativistic Jets

The focus of our study is the jets produced by the AGN and their alignments across distance scales. A typical AGN in a galaxy has a central core of dust and gas that is being accreted onto the central supermassive black-hole($\sim 10^6 - 10^{10}$ solar masses Heckman and Kauffmann (2006)) as seen in figure 1.1. The bright sustained emission from the AGN can be attributed to the strong accretion by the black hole at its midst. While accretion forms the source of most radiation it is largely restricted to the central torus around the supermassive black hole. In classical radio galaxies the accretion process produces two highly collimated jets of ions traveling at relativistic speeds perpendicular to the plane of accretion. The collimation of the jets is due to the spinning accretion disc of the black-hole which twists the magnetic fields in the torus and the jets winding them up. Radio galaxies are classified based on their morphology with Fanaroff and Riley Type I(FRI) , Fanaroff and Riley Type II(FRII) and BL Lacertae Objects. FRII galaxies have higher radio luminosities than FRI galaxies. The FRII galaxy as shown in figure 1.2 is characterized by the highly collimated jets and the hotspots in the regions where the lobes interact with the inter galactic medium. FRI galaxies as shown in figure have more wispy lobe structure and their brightness falls as we move away from the central core to the jets.

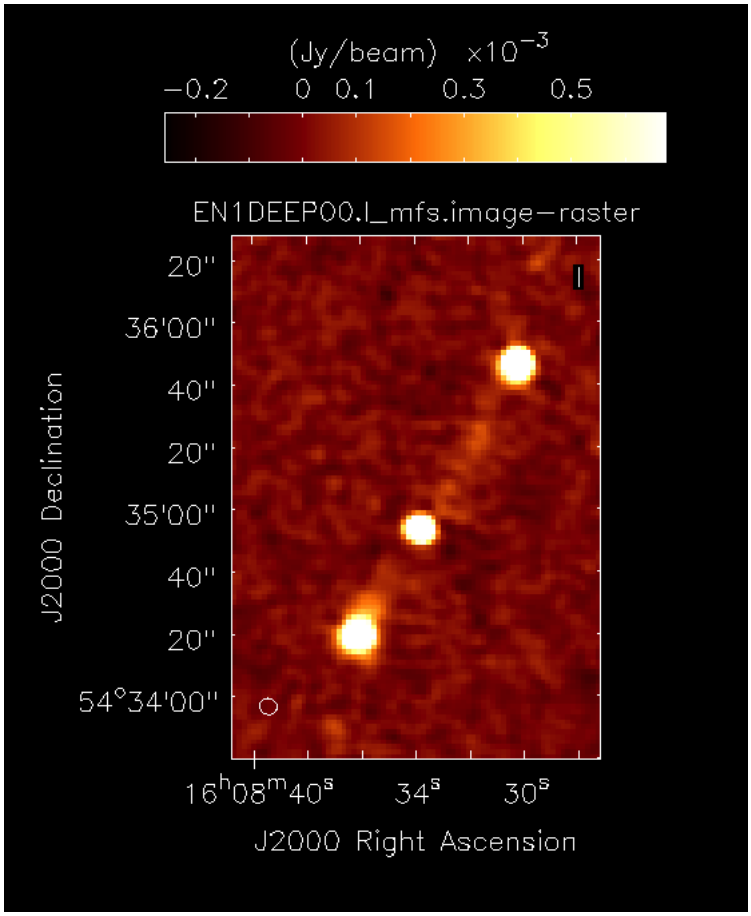

Figure 1.2: A Fanaroff and Riley Type II galaxy from the GMRT ELAIS N1 deep survey. Bright central region and hotspots in the lobes. Jets are highly collimated

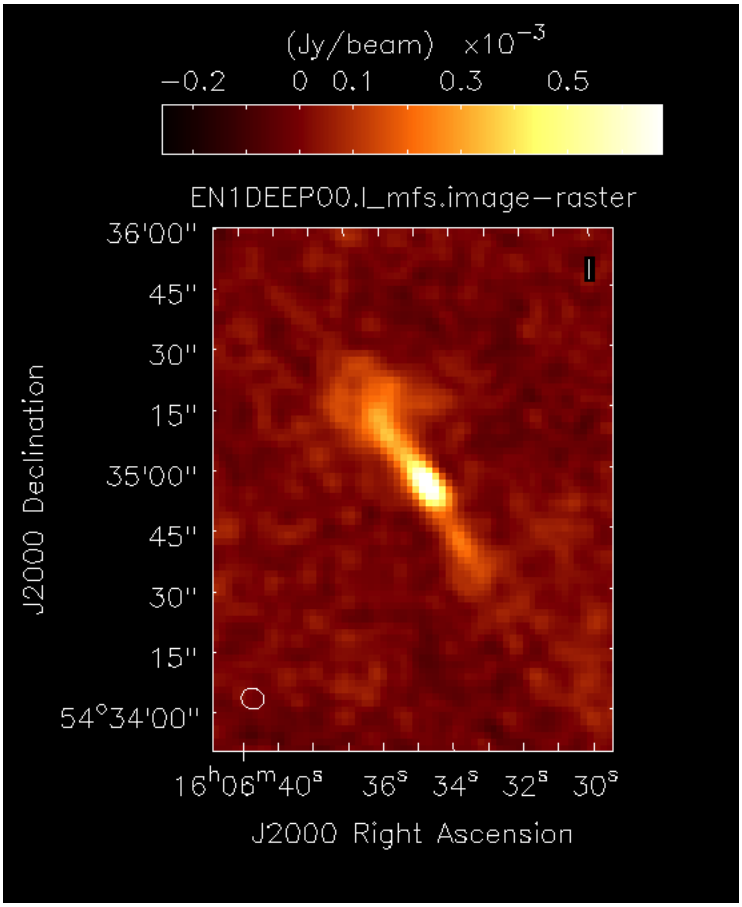

Figure 1.3: A Fanaroff and Riley Type I source from the GMRT ELAIS N1 deep survey. The central core is the brightest region and the brightness falls off as we move towards the lobes. Jets are diffuse and less highly collimated than FR II Galaxies.

1.0.2 Alignments studies in AGN

Evidence for very large scale coherent orientations of quasar polarization vectors was provided by Hutsemékers (1998). They found large scale coherence in polarization position angles around the Northern and Southern galactic poles from a sample of 170 quasars. The angular spread was restricted to 80° rather than the expected 180° if they were all randomly oriented. Despite the initial Kuiper test to show deviations from uniformity proving inconclusive on the complete sample, he proceeded with defining a statistic based on nearest neighbours to extract the alignments in quasar sub-samples particularly around the north and

south galactic poles with 99.99% significance level. Follow up observations by Hutsemékers and Lamy (2001) showed that the alignments in quasars polarization vectors extends to co-moving scales of $1000h^{-1}$Mpc concluding that the alignment of quasar polarization might be correlated with the underlying large scale structure.

Hutsemékers and Lamy (2001) use optical polarization as a probe of AGN large scale alignments. Rusk (1990) show that there is a correlation between the optical polarization and the structural axis of a galaxy. Battye and Browne (2009) show that radio jets are aligned with the optical minor axis, implying that AGN jets position angles are also an equivalent probe of large scale alignments in AGN.

The first goal of this work is to create a very deep, high fidelity image of the ELAIS N1 field of $1deg^2$ at 610 MHz using the Giant Meter-wave Radio Telescope(GMRT). Making a deep field covering 1.2 deg^2 area would require interferometric imaging spanning multiple fields of view over a wide angle. The tendency for the axes of double-lobed radio quasars to be aligned with the electric field vectors of optical polarization in the active galactic nuclei (Stockman et al. (1979)) is known. Hence studying alignments of AGN jets is equivalent to the study of quasar optical polarization. The radio study of AGN jets has the advantage of not being affected by propagation effects which is a major issue to be contended in the case of optical polarization studies. The scale of 1 deg spans a comoving distance of $40h^{-1}$Mpc at redshift $z = 1$ or $64h^{-1}$Mpc at redshift $z = 2$. Studying radio galaxy jet alignments enables us to probe for coherence at comoving scales of up to $40h^{-1}$Mpc at $z = 1$. Large area density of sources allows for us to probe a near complete sample of radio sources in the field.

1.0.3 Challenges of Deep field Imaging

Deep field imaging demands high sensitivities, high dynamic ranges, wide bandwidths and wide field imaging. To achieve thermal noise-restricted images of the order of a few μJy/beam, there is a clear need to account for the varying sky brightness distribution across the bandwidth , and account for the frequency dependent instrumental effects, such as the antenna

primary beam. Recent advances in imaging algorithms in the form of various hybrid projection algorithms such as a W-projection Cornwell et al. (2005), Wide-Band(WB) A-projection Bhatnagar et al. (2013), have laid the framework to be built upon. The frequency dependent sky-brightness distribution can be accounted for by means of the Multi-Term Multi-Scale Frequency Synthesis Rau et al. (2009) The algorithmic framework required to address the wide band, wide field, deep imaging exists in the conjunction of the WB AW-projection algorithm along with the Multi-Term Multi-Scale Frequency Synthesis, while the framework exists, it is as yet untested. As a part of a graduate internship at the National Radio Astronomy Organization, techniques for parallelization of the WB AW-projection along with the Multi-Term Multi-Scale Frequency Synthesis was developed. The parallelization techniques are being tested before primary beam models of the GMRT antennas are introduced. To obtain beam models of the GMRT antennas, observations of a calibrator source were carried out. The measurement and characterization of the primary beams forms an essential portion of the technical developments carried out in this thesis. Primary beam observations and deep field observations of the ELAIS N1 field require large quantities of data to be processed, towards which an automated calibration and imaging pipeline was developed in CASA tailored for the GMRT 610MHz. The automated calibration pipeline required the testing and comparative study of automated flagging algorithms which was carried out.

The subsequent chapters are outlined as:

- Chapter 2 provides an introduction to the basics of radio interferometry and synthesis imaging. The measurement equation methodology is discussed as implemented in radio data analysis software such as the Common Astronomy Software Application(CASA).

- Chapter 3 deals with the challenges of wide field imaging and the required direction dependent corrections such as non coplanar arrays and the effect of the primary beam of the array antennas.

- Chapter 4 provides an overview of the observations and radio data reduction pipeline to produce the GMRT deep field mosaic and measure the primary beam of the GMRT antennas.

- Chapter 5 details the analysis of the AGN jet position angles and the detection of the alignment signal.

- Chapter 6 provides a summary of the conclusions and discusses possible future directions.

Chapter 2

Radio Interferometry & Synthesis Imaging

The ELAIS N1 Deep Radio survey was carried out with the GMRT at 610MHz. The GMRT is a radio interferometric array of 30 antennas that was used to collect the data that is analyzed in this thesis. Radio interferometry and synthesis imaging are the techniques that have made the survey possible. In this chapter I will introduce some fundamental concepts of synthesis imaging and radio interferometry from a theoretical and computational stand point.

2.1 Radio Interferometry

Radio astronomy is the study of the sky at radio wavelengths and has come a long way since the discovery of radio emission from the sky by Karl Jansky (Jansky (1933)). Post second world war radio astronomy became a burgeoning field of study thanks to a lot of advances in radar technology during war-time. The initial thrust was with single dish observations trying to collect as much radio energy as possible with larger and larger dish area. The larger area was also a requisite to obtaining better angular resolution on the sky, which comes from Rayleigh's criterion which dictates that the angular resolution of a telescope is given by

$$\Theta = 1.22\lambda/D \tag{2.1}$$

where D is a measure of the aperture of the telescope and λ is wavelength of observation. For low frequency and large wavelength observations the sizes of the dishes were prohibitive if higher angular resolution was desired. If one desired the resolution of the human eye at radio wavelengths, the diameter of the aperture would have to be many kilometers wide, which was unfeasible both technologically and economically. Sir Martin Ryle proposed a solution

by means of interferometry(Ryle (1955)), where many dishes are utilized to synthesize a much larger effective aperture. This Nobel prize winning discovery changed the way radio astronomy was done and lead to the construction of large array telescopes like the Very Large Array, USA and the Giant Meter-Wave Radio Telescope , India.

2.1.1 Response of an Interferometer

This section of the discussion is derived from Barry Clark's chapter in Taylor et al. (1999) Let us assume that the source in the sky has an intensity distribution $I(S)$ on the celestial sphere of radius R, where s is the source surface area on the sky. Maxwell's equations allows us to superpose the field at a test location by the various source points,

$$E_\nu(r) = \int\int\int P_\nu(R, r)E(R)\, dx\, dy\, dz \tag{2.2}$$

where the integral is over all space. The function $P_\nu(R, r)$ is the propagator that describes how the field at R (source of interest)influences the field at r(observer). Under simplifying assumptions that the source emitting is so far away that the depth information is lost to us and that the celestial sphere is empty but for the source under consideration we can apply Huygens principle to obtain the form of the propagator as,

$$E_\nu(r) = \int \epsilon_\nu(R)\frac{e^{2\pi i\nu|R-r|/c}}{|R-r|}ds \tag{2.3}$$

where ds is an elemental surface area on the celestial sphere and $\epsilon_\nu(R)$ is the electric field at the surface of the source in celestial sphere of radius R. The spatial coherence function is defined as,

$$V_\nu(r_1, r_2) = \langle E_\nu(r_1)E^*_\nu(r_2)\rangle \tag{2.4}$$

where $E_\nu(r_1)$ and $E_\nu(r_2)$ are the electric fields at the point r_1 and r_2 respectively on the detector. Using equations 2.2 and2.3 we get,

$$V_\nu(r_1, r_2) = \langle \int\int \epsilon_\nu(R_1)\epsilon^*_\nu(R_2)\frac{e^{2\pi i\nu|R_1-r_1|/c}}{|R_1-r_1|}\frac{e^{2\pi i\nu|R_2-r_2|/c}}{|R_2-r_2|}ds_1 ds_2\rangle \tag{2.5}$$

where $R_1$and R_2 are the two points on the source from which the electric fields are emanating. For most astronomical sources barring pulsars and masers, source incoherence is a valid assumption. The angular spread of most sources is relatively smaller than the angular coverage of the primary beam of the antenna on the sky. If we make the assumption that the source is spatially incoherent then

$$\left\langle \epsilon_\nu(R_1)\epsilon^*_\nu(R_2)\right\rangle = 0 \tag{2.6}$$

for all $R_1 \neq R_2$, equation 2.5 can then be write as

$$V_\nu(r_1, r_2) = \int\int \left\langle |\epsilon_\nu(R)|^2\right\rangle |R|^2 \frac{e^{2\pi i\nu|R_1-r_1|/c}}{|R_1-r_1|}\frac{e^{2\pi i\nu|R_2-r_2|/c}}{|R_2-r_2|}ds \tag{2.7}$$

If we write s as the unit vector of $R/|R|$ and the observed source intensity as

$$I_\nu(s) = \left\langle |\epsilon_\nu(R)|^2\right\rangle |R|^2. \tag{2.8}$$

Under the assumption that the celestial sphere and the source are very far away from the observer we can neglect terms smaller $|r/R|$ and the surface element ds on the celestial sphere by $|R|^2 d\Omega$ The spatial correlation function $V_\nu(r_1, r_2)$ depends only on $r_1 - r_2$ as given by,

$$V_\nu(r_1, r_2) \approx \int I_\nu(s) e^{-2\pi i\nu s.(r_1-r_2)/c} d\Omega. \tag{2.9}$$

This complex quantity is the time averaged correlation coefficient known as the visibility. An interferometer is made up of an array of spatially separated detectors, and the visibilities are measured for every pair of detectors.

2.1.2 Aperture Synthesis and the Van Cittert-Zernike Theorem

Before exploring the Van Cittert-Zernike theorem there is a clear need to explore the coordinate system of choice. The array is located on the surface of the earth and rotates with respect to a source in the sky due to earth's rotation. The system shown in figure2.1, a right handed (u, v, w) coordinate system as seen from the source. The system is fixed on a

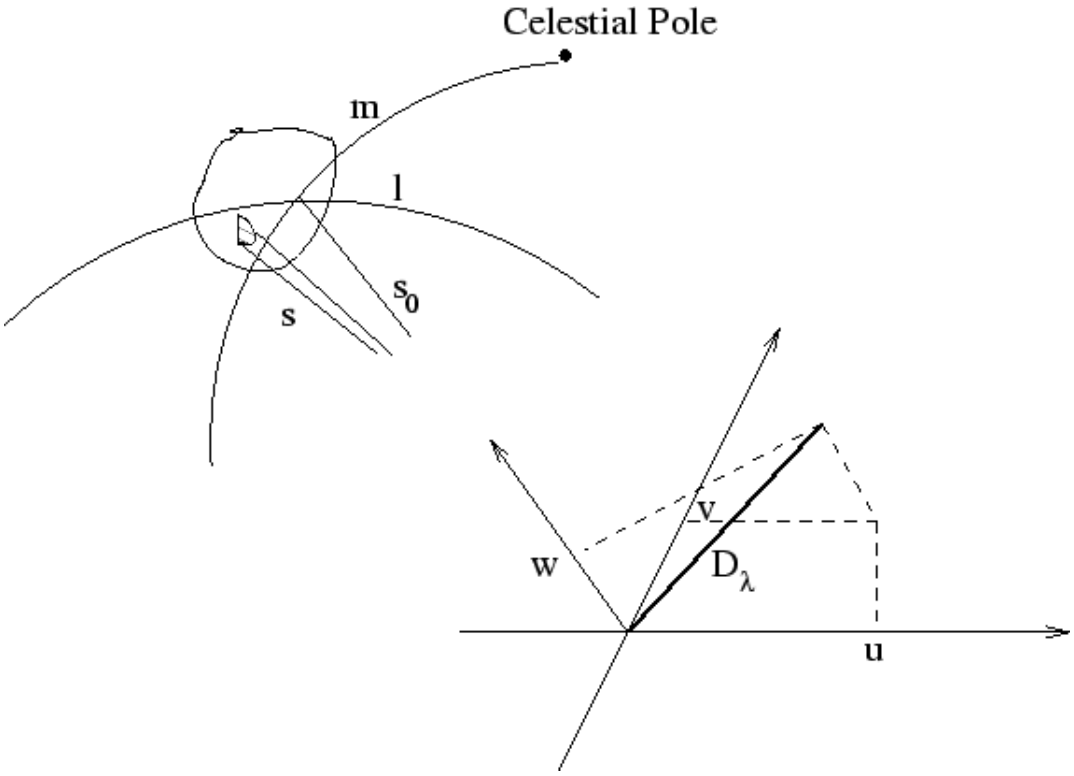

Figure 2.1: The image shows the plane of the array given u, v set parallel to the tangent plane of the celestial sphere at s_0. The vector D_λ is the location of all the array antennas with respect to the reference antenna located at the origin of the uvw plane. The source direction vector s_0 intersects the celestial sphere at coordinates l, m. The phase along any direction s can then be written as $2\pi i\bar{D}_\lambda.(\bar{s} - \bar{s}_0) = 2\pi iw$. The image is courtesy of Chengalur et al. (2003)

reference antenna of the array with the (u, v) plane always parallel to the tangent plane in the direction of the phase centre(s_0) on the celestial sphere along the w axis. The u axis is along the E-W direction and the v axis is along the N-S direction. An E-W array of antennas will always lie on the uv plane and hence is known as a co-planar array.

Van Cittert-Zernike theorem states that the Fourier transform of the mutual coherence function of a distant, incoherent source is equal to its complex visibility. If we choose a favoured coordinate system the vector spacing of the separation variable in the coherence function measured in terms of the wavelength $\lambda = c/\nu$, is $r_1 - r_2 = \lambda(u, v, w)$,. In the same coordinate system the components of the vector s are given in terms of the direction cosines

l, m, n equation 2.9 is

$$V_\nu(u,v,w) = \int I(l,m) e^{-2\pi i(lu+mv+nw)} \frac{dl\, dm}{\sqrt{1-l^2-m^2}}. \tag{2.10}$$

For the celestial sphere there are only two independent co-ordinates so $n = \sqrt{1-l^2-m^2} \approx 1$ which implies that equation 2.10 can be written as

$$V_\nu(u,v,w) = e^{-2\pi iw} \int I(l,m) e^{-2\pi i(lu+mv)} dl\, dm. \tag{2.11}$$

If we define the modified visibility $V_\nu(u,v,w)e^{2\pi iw} = \tilde{V}_\nu(u,v)$ then we obtain the Van Cittert-Zernike theorem, where the visibility is the 2-D Fourier transform of the source intensity,

$$V_\nu(u,v) = \int I(l,m) e^{-2\pi i(lu+mv)} dl\, dm. \tag{2.12}$$

The relationship between the source brightness distribution and observed visibility in the uv plane is a simple Fourier transform relationship. To reconstruct the source brightness distribution we would need to sample $V(u,v)$ for all uv before we can invert the Fourier transform to obtain the sky brightness. To sample the uv plane one can either move the antennas around or we can utilize earth's rotation. Observing the source for prolonged periods of time populates the visibility distribution in the uv plane thanks to the earth's rotation. This can be understood by simply placing yourself at the source and looking at the uv plane of the array which will then rotate around the w axis if the antennas remain stationary forming tracks in the uv plane for each antenna.Technique of using the earth's rotation to sample the uv plane of an interferometric array is known as aperture synthesis. So the visibility is a function of (u,v), if at an instant we observe at multiple frequencies then we would be sampling the uv plane more efficiently. So a large instantaneous bandwidth helps us better sample the uv plane and hence reconstruct the source brightness better. The result of the uv sampling is generally a centrally dominated sampling pattern with a hole in the middle and tapered outer edges. This is called the transfer function of the array or the uv coverage.

Before we venture into calibration it is important to understand the formalism that is used to define a radio interferometer and the Radio Interferometric Measurement Equation that will act as the backbone for the rest of our discussion on interferometry and imaging.

2.1.3 Calibration

Radio waves are affected by instrumental and propagation effects. The process of correcting for the changes due to the instrumental and propagation effects is called calibration. Jones matrices can be used to describe the propagation and instrumental effects for the incident electric field. Suppose we consider our signal, which is quasi monochromatic starting at an arbitrarily distant source is incident on antenna i of our interferometer. The electric field vector can be represented in terms of two orthogonal components as a column vector as given below.

$$\vec{E}_i = [E^r, E^l]_i^T \tag{2.13}$$

the medium of propagation and receiver instrumentation effect a change on the propagating vector. The effect is linear and hence can be described by a corresponding 2×2 complex matrix J_i such that

$$E_i^{'} = J_i E_i$$

If we consider another antenna j with a signal matrix E_j and a corresponding Jones matrix J_j then we can write the observed cross correlated voltage patterns in a simple linear matrix form as

$$V_{ij} = 2 J_i \langle E_i E_j^{\dagger} \rangle J_j^{\dagger}$$

The bracketed quantity here is intimately related to the definition of the Stokes parameters, for a more detailed explanation see Born and Wolf (1999). Sault et al. (1996) showed that the relation between the quantities $2\langle E_i E_j \rangle$ and the Stokes parameters through the sky brightness matrix is

$$2\langle E_i E_j \rangle = I^{sky}$$

All calibration corrections can be classified as direction-dependent and direction independent corrections. Direction independent effects are effects that are caused by the antenna, receiver electronics or feed configuration. The direction independent effects for an antenna i can be represented by the 2×2 matrix product of the complex antenna gains G, and polarization leakage D. The Jones matrix for direction independent calibration is

$$J_i = [G_i D_i] \tag{2.14}$$

Where

$$G_i = \begin{bmatrix} g_r & 0 \\ 0 & g_l \end{bmatrix}, \; D_i = \begin{bmatrix} 1 & D_r \\ D_l & 1 \end{bmatrix}$$

The outer product is then

$$[G_i \otimes D_i] = \begin{pmatrix} g_{ri}g^*_{rj} & g_{ri}g^*_{rj}D^*_{rj} & g_{ri}g^*_{rj}D_{ri} & g_{ri}g^*_{rj}D_{ri}D^*_{rj} \\ g_{ri}g^*_{lj}D^*_{lj} & g_{ri}g^*_{lj} & g_{ri}g^*_{lj}D_{ri}D^*_{lj} & g_{ri}g^*_{lj}D_{ri} \\ g_{li}g^*_{rj}D_i & g_{li}g^*_{rj}D_{li}D^*_{rj} & g_{li}g^*_{rj} & g_{li}g^*_{rj}D^*_{rj} \\ g_{li}g^*_{lj}D_{li}D^*_{lj} & g_{li}g^*_{lj}D_{li} & g_{li}g^*_{lj}D^*_{lj} & g_{li}g^*_{lj} \end{pmatrix} \tag{2.15}$$

Before we venture into calibration the theoretical and practical basis are in the form of the radio interferometric measurement equations. The radio interferometric measurement equations are an application of the Jones and Mueller matrix formalism introduced in radio astronomy by Hamaker et al. (1996) and Sault et al. (1996). These form the basis of modern day interferometry.The measurement equation for one baseline for a unit frequency per unit time is given by,

$$V^{obs}_{ij} = [K_{ij}] \int [K^{DD}_{ij}] I^{sky}(s) e^{-2\pi i b.\sigma/\lambda} d\Omega \tag{2.16}$$

This is the measurement equation for a single baseline, where K_{ij} is the gain matrix that encodes the antenna and baseline based effects, K^{DD}_{ij} is the gain matrix that encodes the direction dependent effects. For an array of n antennas there are $n(n-1)/2$ unique baseline pairs which make measurements at the same time. The complete measurement equation for the array can then be written in matrix form each having $n(n-1)/2$ visibility vectors.

Let $I^{sky}_{m\times 1}$ be the sky image and $V^{obs}_{n\times 1}$ be the visibility vector of the n observed visibilities. $S_{n\times m}$ is the projection vector or the discrete sampling function for a given UVcoverage that maps m observed uv points to n visibility samples. The measurement equation in block matrix form can be written as

$$V^{obs}_{cn\times 1} = [K_{cn\times cm}][S_{cn\times cm}][F_{cm\times cm}][K^{DD}_{cm\times cm}]I^{sky}_{cm\times 1} \tag{2.17}$$

Where c is the number of polarizations (1, 2 or 4) , henceforth we shall set $c = 1$. $F_{m\times m}$ is the Fourier transform operator. In the spatial frequency domain the equation can be recast as

$$V^{obs}_{n\times 1} = [K_{n\times m}][S_{n\times m}][G_{m\times m}]I^{sky}_{m\times 1} \tag{2.18}$$

where $[G_{m\times m}] = [F_{m\times m}][K^{DD}_{m\times m}][F^{\dagger}_{m\times m}]$ is the convolution operator in the spatial domain. The † symbol is used to denote the conjugate transpose or the adjoint of a matrix henceforth. The rest of the discussion on calibration and imaging follows Rau et al. (2009) which forms the algorithmic basis for the imaging and calibration in the Common Astronomy Software Application(CASA, Jaeger (2008)).

The measurement equation for a single correlation accounting for only the direction independent effects in matrix form is,

$$V^{obs}_{n\times 1} = [K_{n\times m}][S_{n\times m}F_{m\times m}]I^{sky}_{m\times 1} \tag{2.19}$$

for the cross correlation rr, the complex gains per antenna i is be given by $[G_i] = g^r_i$. Then,

$$K_{ij} = G_i \otimes G_j = g^r_i g^{*r}_j \tag{2.20}$$

is a scalar and $[K_{ij}]$ is a diagonal matrix. The unknowns in equation 2.19 are the sky brightness I^{sky} and the complex gain product for all the visibilities K. The correction to obtain the calibrated visibilities is then an exercise in computing the inverse of the complex gain matrix $[K_{ij}]^{-1}$. The standard calibration procedure is to use a source whose flux and

structure is known *a priori*. For the calibrator source then we known the true visibilities $V_{n\times1}^{model}$. We can then solve the equation

$$V_{n\times1}^{obs} = [K_{n\times m}]V_{n\times1}^{model} \tag{2.21}$$

The $[K_{ij}]^{-1}$ is then applied to the observed visibilities to obtain the corrected visibilities.

$$V_{n\times1}^{corr} = [K_{ij}]^{-1}V_{n\times1}^{obs}. \tag{2.22}$$

Using equations 2.19 and 2.22 we can write the measurement equation post calibration as

$$V_{n\times1}^{corr} = [S_{n\times m}F_{m\times m}]I_{m\times1}^{sky}. \tag{2.23}$$

The corrected visibilities now form the basis for the next step, namely imaging.

2.1.4 Imaging

The purpose of imaging is to obtain an estimate of the sky brightness I^{sky} . To reconstruct the sky brightness distribution, we perform a weighted least square estimate,

$$[F^{\dagger}S^{\dagger}WSF]I_{m\times1}^{sky} = [F^{\dagger}S^{\dagger}W]V_{n\times1}^{corr} \tag{2.24}$$

where $W_{n\times n}$ is a diagonal matrix of signal to noise based measurement weights. $S^{\dagger}$ denotes the mapping of measured visibilities onto a spatial grid. In the above equation the the left hand side of the equation gives the imaging properties of the instrument while the right hand side represents the Fourier transform of the calibrated visibilities to give us a raw image. The raw image produced from the direct Fourier transform of the visibilities is known as the dirty image. When

$$V_{n\times1}^{corr} = \vec{1}_{n\times1} \tag{2.25}$$

for a point source at the phase centre of the interferometer, the right hand side of the equation above gives the point spread function I^{psf} or the impulse response function. The dirty image is a convolution of the true image I^{sky} with the point spread function of the interferometer and a simple deconvolution would give us the true dirty image.

Since S represents the incompletely sampled spatial frequencies, the hessian $[F^{\dagger}S^{\dagger}WSF]$ cannot be inverted directly to obtain a linear deconvolution operator. An iterative Newton-Raphson approach is implemented as follows.

- Initialize the model image I_0^m to zero or to a model that represents *a priori* information about the true sky.

- Major Cycle: Compute the $\nabla\chi^2$ residual image,

$$I^{res} = \{[F^{\dagger}S^{\dagger}W][V^{corr} - [SF]I_i^m]\} \tag{2.26}$$

  The forward transform $V^m = [SF]I_i^m$ is used as a prediction that would be measured for the sky model and the residual visibilities are computed as

$$V^{res} = V^{corr} - V^{mod} \tag{2.27}$$

  The reverse transform $I^{res} = [F^{\dagger}S^{\dagger}W]V^{res}$ computes an image from a set of visibilities. The weight function W is applied to the visibilities before *Gridding* them onto a regular grid of spatial frequencies. The visibilities are then Fourier inverted to give us I^{res}.

- Minor Cycle: Is when the model image is updated by applying an operator T to the $\nabla\chi^2$ image.

$$I_{i+1}^m = I_i^m + T(I^{res}, I^{psf}) \tag{2.28}$$

  T represents the non-linear deconvolution of the PSF from I^{res} while filling in measured spatial frequencies for complete image reconstruction. The interferometer only samples certain spatial frequencies as we know and the rest

are reconstructed by extrapolation, particularly for the null space of the UV plane.

- Repeat steps from the major cycle until convergence is achieved. The convergence criteria can be I^{res} is noise-like or that the transformation T can no longer reliably be extracted from I^{res} .

- The final I^m is restored first by smoothing it to the maximum angular resolution of the instrument to suppress the artifacts arising from unconstrained spatial frequencies beyond the measured range and by adding the final I^{res} to preserve any undeconvolved flux.

The iterative Newton Raphson approach is also known as the CLEAN algorithm originally proposed by Högbom (1974). The algorithm as discussed earlier is a modification to the original algorithm by Clark (1980)

2.1.4.1 Weighting

The aim of weighting the visibilities before imaging is to alter the shape of the PSF. The most trivial case of weighting is to give equal weights to all the sampled visbilities, and is called Natural weighting. Natural weighting preserves the instrument's peak sensitivity, making it ideal for the detection of low signal to noise sources. The non-uniform sampling of the UV plane causes the PSF to have a large main lobe and high side lobes. The other form of weighting of visbilities is to give all the gridded visibilities uniform weight. So if a grid cell contained N points the weights for each of the points would then be $1/N$. This ensures that each measured spatial frequency is equally weighted, which causes the peak sensitivity to be lowered. Robust Weighting creates a PSF that smoothly varies between Natural and Uniform weighting based on the signal to noise ratio of the measurements and a tuneable parameter that defines a noise threshold. The final imaging weights are a combination of the weighting scheme W^{pc} and weights based on the measurement noise W(usually inverse

of the noise variance) based weights, such that $W^{im} = W^{pc}.W$. The hessian becomes a convolution operator with the preconditioned PSF given by

$$I^{psf} = diag[F^{\dagger}S^{\dagger}W^{im}] \tag{2.29}$$

2.1.4.2 Gridding

In order to be able to use the Fast Fourier Transform algorithm on the observed visibilities, the sampled UV points must be transferred onto a regular spatial grid. This process is known as gridding. Gridding interpolation is carried out as a convolution operator. So each gridded visibility is convolved with some gridding convolution function $C(u, v)$. The form of the convolution function plays a role in macroscopic properties of the resulting image. Some common gridding convolution functions are the pillbox, truncated sinc function and spheroids.

Each weighted visibility is first multiplied with a prolate spheroidal function P_s centered on its true location. The correction for this convolution is a multiplicative correction in the image domain which is carried out to remove the gridding convolution function. P_s can be thought of as a diagonal matrix representing the prolate spheroidal function. The corresponding gridding convolution function is given by

$$G^{gc} = [F(F^{\dagger}P_s)F^{\dagger}] \tag{2.30}$$

which is equivalent to multiplication in the image domain

$$I^{wt}_{gc} = [F^{\dagger}P_s]_{m\times m} \tag{2.31}$$

The normalized dirty image and PSF are,

$$I^{\{dirty,psf\}}_{m\times 1} = w^{-1}_{sum}[I^{wt}_{gc}]^{-1}[F^{\dagger}G^{gc}S^{\dagger}W^{im}]V^{\{corr,1\}}_{n\times 1} \tag{2.32}$$

where $w_{sum} = trace(W^{im})$ is the normalization factor of the PSF. This is practical implementation of the reverse transform of the major cycle and I^{dirty} is the initial residual image

used to start the imaging iterations. The model image obtained at the end of each Minor cycle is used in the forward transform as

$$V^m_{n\times 1} = [SG^{gc}F][I^{wt}_{gc}]^{-1} I^m_{m\times 1} \tag{2.33}$$

These forward transform calculations are computationally expensive and imaging algorithms usually tailor the Major and Minor cycles to perform trade-offs between number of iterations, accuracy and performance.

Chapter 3

Challenges of Wide-field Imaging

The imaging formalism given in the earlier chapter dealt with the standard imaging procedure. In this chapter the issues with low frequency imaging particularly those of direction dependent corrections and imaging is discussed.

3.1 Imaging with Direction Dependent Corrections

Direction-dependent effects can also be cast in a 2×2 matrix product of the antenna illumination pattern E, parallactic angle effects P, the tropospheric and ionospheric effects, and Faraday rotation F, to give

$$J_i = [EPF] \tag{3.1}$$

The effect on each baseline ij can then be described by the outer product of the antenna based Jones matrices $J_i$and J_j as

$$K_i = [J_i \otimes J_j^{\dagger}] \tag{3.2}$$

In a general form the direction dependent effects of a calibrated array can be written as

$$V^{obs}_{n\times 1} = [S_{n\times m}][G^{dd}_{m\times m}]V^{sky}_{m\times 1} \tag{3.3}$$

where $G^{dd}_{m\times m}$ encodes the gains due to various direction dependent effects. We can use a formulation as in equation 3.3 to suggest that an FFT based forward and reverse transform can account for the direction dependent effects for a carefully constructed G^{dd} operator. Non co-planar arrays and the primary beam rotation for an alt-az mounted antenna are two instances for which direction dependent gains can be accounted for using the w projection(Cornwell et al. (2005)) and A projection(Bhatnagar et al. (2013), Bhatnagar et al.

(2008)) algorithms respectively. In subsequent sections the physical effects of non coplanar arrays and the antenna primary beam effects along with the required corrections are explained.

3.2 Non Co-Planar Arrays

Earlier during our discussion of the Van Cittert-Zernike theorem we showed the basic radio interferometric equation 2.10. The far-field pattern of the antenna or the primary beam, $A(l,m)$ when taken into account modifies the radio interferometric equation to,

$$V_\nu(u,v,w) = \int I(l,m)A(l,m)e^{-2\pi i(lu+mv+w\sqrt{1-l^2-m^2})}\frac{dl\,dm}{\sqrt{1-l^2-m^2}} \tag{3.4}$$

here (u,v,w) is the coordinate spacing of the antennas, and (l,m,n) the direction cosines of the coordinate system. Like in the previous case, we can set $A(l,m)$ to be 1 at the moment. Later parts of this chapter are dedicated to exploring the effects of the primary beam on imaging, so we shall revisit this aspect later. The above equation in its current form is not yet a Fourier transform relation. The assumption that $\sqrt{1-l^2-m^2} \simeq 1$, gave us the 2D Fourier relation of the Van Cittert-Zernike theorem. This approximation is valid only at the phase centre of the image. The error gets larger as one moves out radially from the phase center of field. For a wide field of view the error becomes significant towards the field edges and to image the entire field an alternate strategy is needed. One approach is to treat n as an independent variable. This gives us an image volume where (u,v,w) have Fourier conjugate variables (l,m,n) which can be written as

$$F(l,m,n) = \int\int\int V(u,v,w)e^{-2\pi i(ul+vm+wn)}du\,dv\,dw \tag{3.5}$$

substituting for $V(u,v,w)$ from equation 3.4

$$F(l,m,n) = \int\int\left\{\int\int\int \frac{I(l',m')}{\sqrt{1-l^2-m^2}}e^{-2\pi i(u(l'-l)+v(m'-m))}e^{-2\pi i(w\sqrt{1-l'^2-m'^2}-n))}du\,dv\,dw\right\}dl'\,dm' \tag{3.6}$$

Using the fact that

$$\delta(l' - l) = \int e^{-2\pi i u(l'-l)} du \tag{3.7}$$

gives,

$$F(l, m, n) = \int\int \frac{I(l', m')}{\sqrt{1 - l^2 - m^2}} \delta(l' - l)\delta(m' - m)\delta(\sqrt{1 - l^2 - m^2} - n) dl'\, dm' \tag{3.8}$$

This equation relates the 2D sky brightness distribution $I(l, m)$ with the 3D Fourier inversion of the visbilities given by $F(l, m, n)$ which corresponds to an image volume.

$$F(l, m, n) = \frac{I(l, m)\delta(\sqrt{1 - l^2 - m^2} - n)}{\sqrt{1 - l^2 - m^2}} \tag{3.9}$$

To understand the 3D formulation, consider the celestial sphere enclosed by the image volume $I(l, m, n)$ with the top most plane being a tangent to the celestial sphere. Then equation 3.9 states that only parts that lie on the surface of the celestial sphere correspond to that of the image volume as shown in figure 3.1. For all other points on the celestial sphere the emission needs to be radially projected onto the tangent image plane to obtain the true value of the emission.

The most logical method for recovering the true sky brightness is to perform the 3D Fourier transform $V(u, v, w)$. A 3D Fourier transform requires that we also Nyquist sample the w axis. For most observations Nyquist sampling is not satisfied on the third axis which causes severe aliasing. In practice, the transform on the third axis is usually done using the direct Fourier Transform on the ungridded data. The size of the synthesized beam in the direction n is comparable to that in the other two directions and is given by $\approx \lambda/B_{max}$ where B_{max} is the longest projected baseline length. Therefore the separation between the planes along n should be $\leq \lambda/2B_{max}$. The distance between the tangent plane and the sky plane points separated by θ from the phase centre is given by $1 - cos\theta \approx \theta^2/2$. For critical sampling the number of planes in n would be the ratio of the distance between the tangent plane and the sky plane with the critical number of planes is

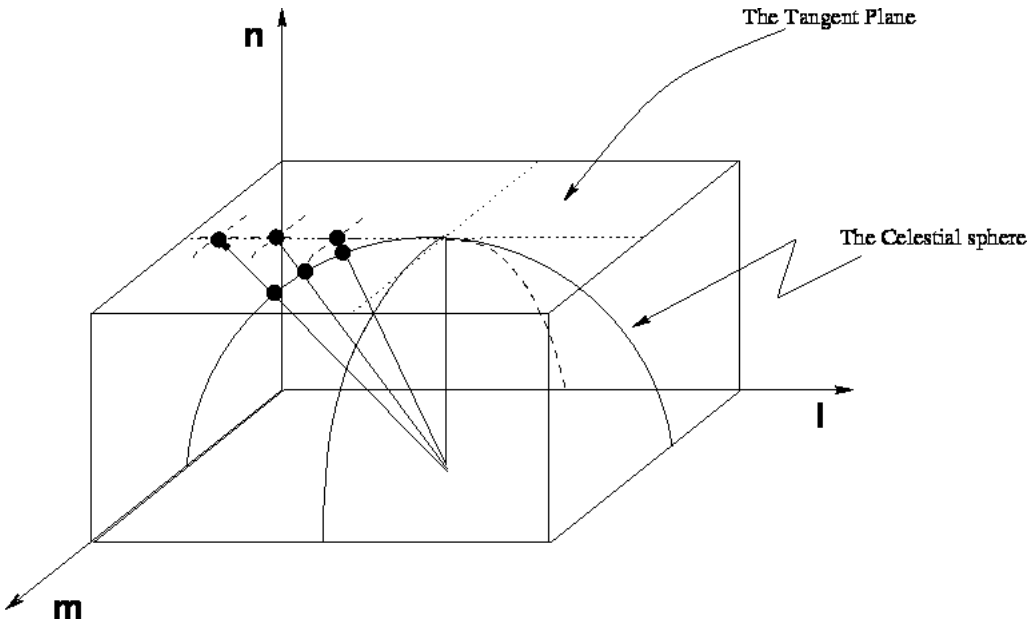

Figure 3.1: Graphical representation of the geometry of the Image volume and the celestial sphere. The point at which the celestial sphere touches the first plane of the Image volume is the point around which the 2D image inversion approximation is valid.Image courtesy of Chengalur et al. (2003)

$$N_n \approx (\theta^2/2)/(\lambda/2B_{max}) \approx B_{max}\theta^2/\lambda \tag{3.10}$$

The 3D Fourier Transform is performed followed by the projection of the celestial sphere on the image plane to obtain the true sky brightness image. This methodology is called w projection and is incorporated in CASA as a part of the CLEAN task. For the 610MHz GMRT data that forms the basis of this thesis 256 planes were used while imaging to account for the non-coplanarity of the data.

3.3 Primary Beam of the Antenna

In optical astronomy the use of mirrors to focus the light towards the detectors finds a direct counter-part in the parabolic radio dish, in the case of radio astronomy. The antennas in an interferometric array act as collection centres for the radio waves. The metallic dish reflects the radio waves towards the prime focus where the receiver feeds are placed to observe the

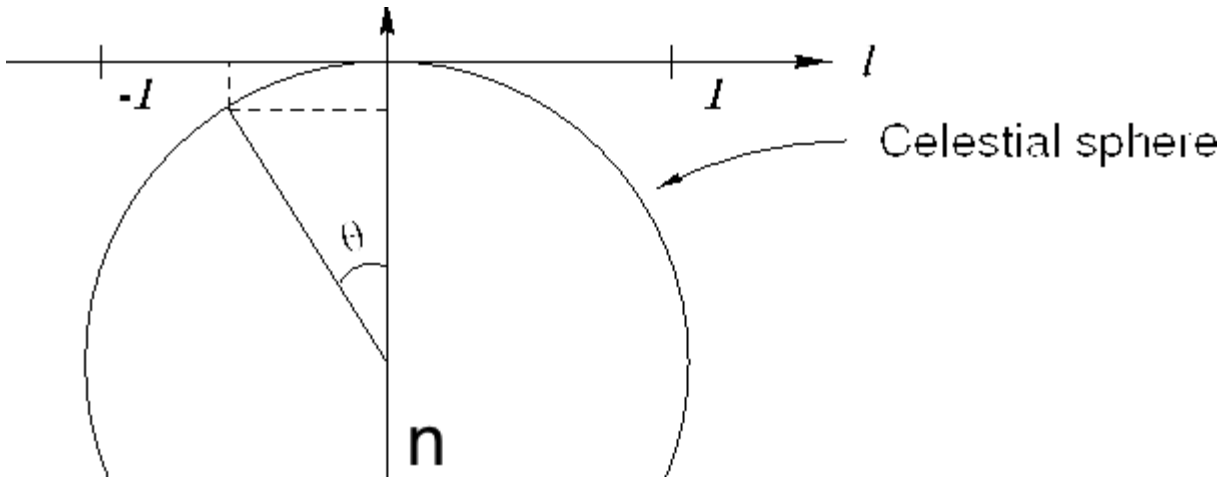

Figure 3.2: Graphical representation of the angular difference in the sky plane and tangent plane away from the pointing centre. Image courtesy of Chengalur et al. (2003)

incident radio waves as is the case for the GMRT. In such a case, the radio dish serves to collect and direct radiation in addition to restricting the field of view(FOV). The FOV of antenna is given by

$$FOV \sim \lambda/D \tag{3.11}$$

where D is the diameter of the dish and λ is the wavelength of observation.

The GMRT antennas are 45m dishes made of a wire mesh and 4 prime focal receiver feeds that enable observations at 150MHz, 230MHz, 325MHz, 610MHz and 1400MHz. The collection area of the antennas can be expressed in terms of an effective area A. Consider a point source of brightness $I(\nu, l, m)$ $\mathrm{Wm^{-2}Hz^{-1}ster^{-1}}$, where l, m are direction coordinates on the sky. The power collected over a solid angle $d\Omega$ per unit bandwidth $d\nu$ is given by,

$$P = A(\nu, l, m)\, I(\nu, l, m)\, d\Omega\, d\nu \tag{3.12}$$

where $A(\nu, l, m)$ is the far field voltage pattern of the antenna also called the antenna primary beam.

The effective area is also a function of the sky coordinate and the frequency of observation. The directional effective area then describes the sensitivity of the antenna to stray radiation. The effective area for the parabolic antenna along the pointing direction is a circular aperture

cross-section. The Fourier transform of the cross section is called the antenna aperture illumination pattern or the primary disc. Since the circular aperture is of a finite size the Fourier transform is a diffraction pattern known as the airy disc.

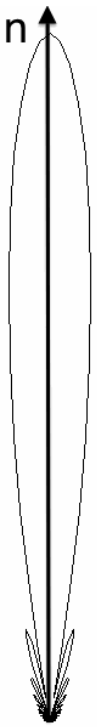

Figure 3.3: A typical primary beam of a single dish antenna. The beam is azimuthally symmetric and a slice along the n axis is shown above. There is significant forward gain along the direction of the phase centre in the forward direction.

The power pattern of an individual dish telescope is given by $|F(l,m)|^2$ where $F(l,m)$ is the complex far-field voltage pattern for the antennas. Perfectly parabolic antennas produce circular beams due to azimuthal symmetry. Accurate knowledge of the primary beam is required to correct for the rotation of a non circular beam during deconvolution. Figure 3.3 shows an azimuthal slice of a symmetric beam along the pointing direction. The beam is normalized by the peak value of the power in the main lobe which then provides the divisive correction for the image plane fluxes in a radio image.

A typical antenna structure includes the main parabolic aperture and the feeds at the prime focus held up by support structures. The support structures are large enough to cause

radio waves to diffract around them. To accurately map the primary beam and illumination pattern it is important to account for the structure parameters while computing the primary beam. The support structures block the aperture, casting a shadow that affects the beam shape directly in addition to the aperture efficiency as detailed in figure 3.4

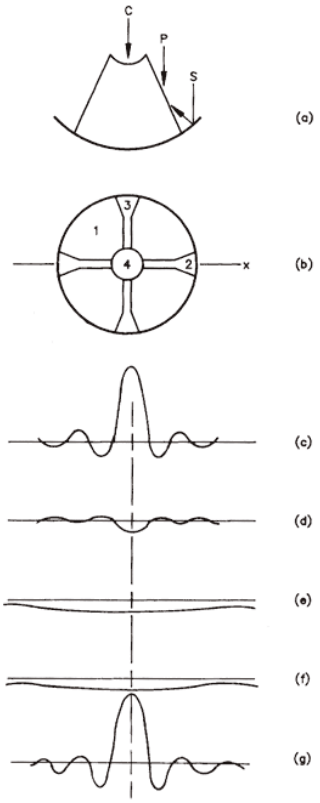

Figure 3.4: The figure illustrates the various parts of a parabolic reflector and analyses the different parts of the structure separately. The regions 1, 2, 3 and 4 are antenna structures marked in (b). The Fourier Transform of the unblocked aperture is shown in (c). While (d),(e) and (f) show the Fourier Transform of the parts marked 2, 3 and 4, shown in negative as they are blockages. (g) gives the sum of the Fourier Transforms to denote the actual measured beam. It's worth noting that the side lobes are transformed and the aperture illumination is modified. (g) is measured by performing holography of the antenna. The image is courtesy of Prof. Dale.E.Gary(web.njit.edu/∼gary/728/lecture9.html)

The primary beam can be measured for the array dishes by performing a grid observation around a point source of known flux density. Corrections for the primary beam are possible only with the measured beam of the antenna. In our attempt to obtain the true GMRT primary beam we performed a square grid observation of the GMRT antennas cen-

tred on a calibrator source on various occasions. The forthcoming chapter will describe the observations, analysis and the beam shapes obtained and the corrections currently being implemented.

Chapter 4

Observations and Data Processing

This chapter outlines the data collection and imaging of the ELAIS N1 deep field. Automating the data processing was an important technical goal of this work. A complete description of the data pipeline developed is discussed, covering data flagging, calibration and imaging. The latter portion of the chapter will introduce the data collection and processing of the GMRT primary beam observations which is the other important technical goal of this work.

4.0.1 Giant Meter-Wave Radio Telescope

The Giant Meter Wave Radio Telescope(GMRT) is located 80km from Pune, India at a site called Khodad in the Narayangaon area. GMRT consists of 30 steerable parabolic dishes of 45m diameter each spread over distances of up to 25km. Refer to figure 4.1 for antenna positions. Fourteen of the 30 dishes are located in the central square of 1sqKm area and the remaining 16 are spread out along 3 arms to provide a 'Y-Shaped' configuration over a much larger region, providing a maximum interferometric baseline of nearly 30 Km. In effect the array will act as the equivalent of a 30km diameter dish in terms of the angular resolution. The highest achievable angular resolution of the array is about 2 arcsec at 1.4GHz or $\sim$ 5 arcsec at 610MHz. The GMRT operates in six different frequency bands centred around, 50, 153, 233, 325, 625 and 1420MHz in dual polarization mode providing a maximum of 256 channels at 8, 16 and 32MHz bandwidth respectively.

4.0.2 Deep Field Observations and Data Processing

The ELAIS N1 is a legacy deep field with multi wavelength data available from Spitzer, Planck, Herschel satellites, with ground based follow ups in optical wavelengths providing photometry and spectrometric redshifts. The field has been studied in the past in the radio

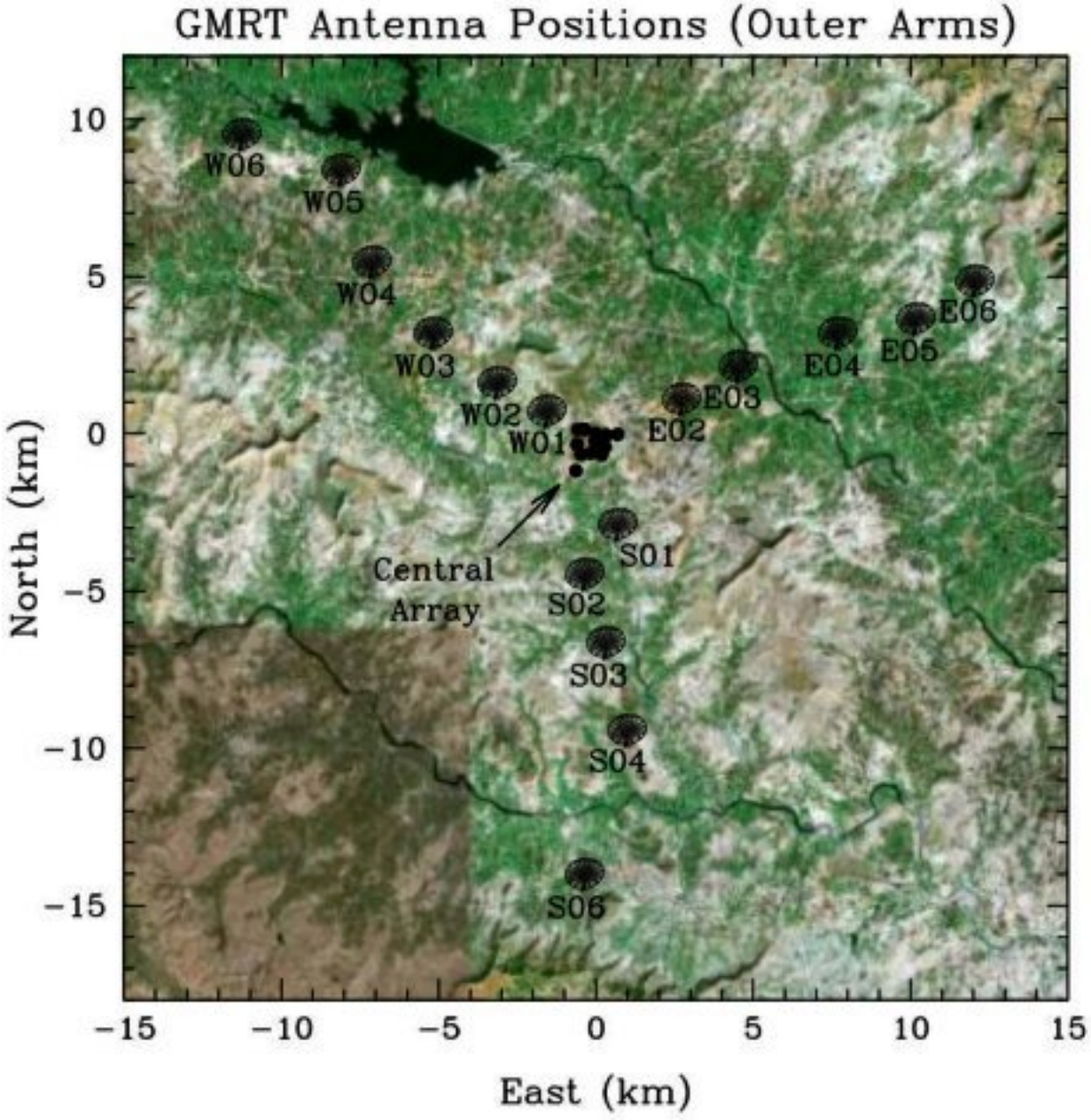

Figure 4.1: GMRT Antenna Positions of the outer arm. The central array has 14 antennas in the central square kilometre of the array.

(refer table 4.1) using the GMRT, VLA and DRAO Synthesis Telescope at 610MHz and 1.4GHz. These prior studies and extensive multi wavelength data were essential in choosing the ELAIS N1 as our target deep field. The proposal to study the field suggested a two pronged approach, one that would cover the 2 square degrees to complement the wide-area surveyed by the satellites and the other was to probe deeper in a smaller region around the field centre three times deeper in sensitivity to $6\mu Jy$. The ELAIS N1 deep field pointings were centred on the field center of the Spitzer extragalactic representative volume survey. A plot of the pointings overlaid on the 1.4GHz image of Taylor et al. (2007) is shown in figure 4.2. A filled-centre hexagonal mosaic pointing configuration of the pointings was chosen to provide nearly uniform sensitivity across the central regions of the map out to the half power point. The observations were carried out in full polarimetric mode at 615MHz frequency and a bandwidth of 32MHz divided into 256 channels. Each field was observed for 30 hours in 3 sets of 10 hour runs each. For the observations, 3C286 was used as the primary flux, bandpass and polarization position angle calibrator and was observed at the start and middle of each 10 hour observing run. 1549+506, a calibrator from the EVLA calibrator manual, was used as the phase and instrumental polarization calibrator and was observed for a period of 8 minutes for every 30 minutes on source. We had good parallactic angle coverage over 10 hours of Hour Angle during the observations allowing for instrumental polarization calibration with 1549+506. Accounting for overheads we have a total of 7.5 hours on source for each observing run of 10 hours. So the cumulative time on source for the 7 pointing mosaic is 157.5 hours. The sensitivity of the telescope is given by,

$$\sigma = \frac{\sqrt{2}T_s}{G\sqrt{n(n-1)N_{IF}\triangle\nu\tau}}$$

Where the system temperature $T_s \simeq 92K$, and the antenna gain $G \simeq 0.32KJy^{-1}$ all values and formulae taken from the GMRT website[1], n is the number of working antennas which is typically 29 due to maintenance and painting. $N_{IF} = 2$ is the number of sidebands,

[1] $http://gmrt.ncra.tifr.res.in/gmrt_hpage/Users/doc/manual/UsersManual/node13.html$

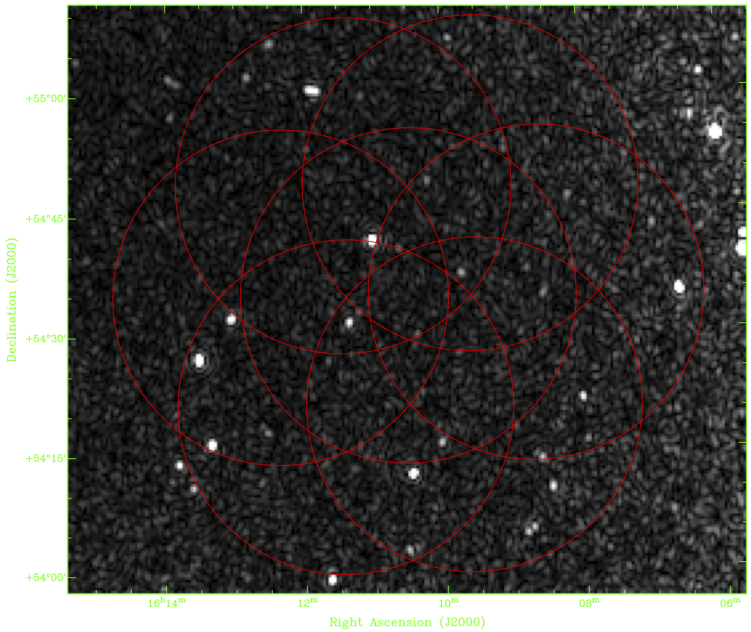

Figure 4.2: Deep Field Pointings overlaid on the DRAO image of Taylor et al. (2007)

$\triangle\nu = 13.75$MHz is the effective bandwidth per sideband, and $\tau = 81000s$ is the total on source integration time. This gives a value of $\sigma = 6.4\mu Jy$ as the theoretical sensitivity that can be achieved as against the observed sensitivity of $\sigma = 10\mu Jy$ before primary beam correction.

The data were obtained in the native binary Long Term Accumulation(LTA) format provided by the GMRT software correlator. The online flags were applied to the data in the native LTA format, which are converted to the UVFITS data format using observatory provided software LISTSCAN and GVFITS. The resulting fits files were then stored and transferred to the University of Calgary for further processing with a pipeline scripted using the Common Astronomy Software Application(CASA).

4.0.2.1 Radio Frequency Interference

With increasing use of the frequency spectrum and human habitation around the GMRT there have been increasing instances of radio frequency interference(RFI). Thirty hours of data from the original time allocation, were lost to intense RFI, for which compensatory

Survey	Frequency	Sensitivity	Area
DRAO - Taylor et al. (2007)	1.4 GHz	210μJy/beam	~2.1 deg^2
GMRT - Garn et al. (2008)	610 MHz	270 μJy/beam	9 deg^2
GMRT - Sirothia et al. (2009)	325 MHz	40 μJy/beam	7.7 deg^2
VLA - Banfield et al. (2011)	1.4GHz	87μJy/beam	1 deg^2

Table 4.1: Radio Observations of the ELAIS N1

director discretionary time was sought and obtained. There is also RFI signal contamination to a moderate extent throughout the remaining days of observations. The first problem of pipelining the data were to find an appropriate automated flagging routine given the large amount of data. A test was run to compare the three most common open source flagging algorithms, TFCROP and RFLAG in CASA, and the Low Frequency Array(LOFAR) flagger, Offringa (2010). The test was performed to see which of the algorithms would perform most efficiently whilst flagging least amount of good data. This was done by comparing the percentage of visibility data points flagged to achieve complete flagging of the RFI as visible to the naked eye in an average baseline.

TCROP [2] algorithm by Urvashi Rau is a thresholding based algorithm that models the bandpass while fitting an n^{th} order polynomial to the visibility data as a function of frequency and time. Cut-off parameters in time and frequency are then used to flag out outliers. The algorithm performs very well with narrow band RFI in time and frequency, with reduced detection performance for RFI at channel and band edges. The task also flags the four cross correlations separately, which is essential in identifying RFI which show up only in the RL and LR correlations and not in RR and LL correlations. When coupled with the task to extend the flags across polarization adds to the robustness of the TFCROP flagging routine.

RFLAG algorithm is an adaptation of a long standing autoflagging algorithm developed by Eric Greisen. The algorithm is a statistical flagging algorithm that samples the visibility data and flags outliers that are outside the specified variance cutoff. The parameters that were ideal for the purposes of flagging the GMRT data are furnished below

[2]http://www.aoc.nrao.edu/ rurvashi/TFCrop/TFCropV1/node2.html

LOFAR Flagger has strategy files that can be created expressly for the purpose of pipelining and batch data processing. A strategy file was created for the GMRT data after extensive experimentation with the threshold parameters, which are not intuitive unlike RFLAG and TFCROP. The flagger was originally C based and could not complete a call from within CASA with regards to some issues of not having a proper exit code. This bug was reported by our group and has been rectified in the current version of the software. With the software now accessible from within the CASA ipython interface it was then possible to pipeline our data such that flagging would be carried out by the LOFAR flagger from within the python pipeline running in CASA. The results of the LOFAR flagger were impressive, it was both robust and fast and flagged the minimum number of visibility data points per baseline. The flaggers were compared by testing them with real GMRT ELAIS N1 Deep field data. Days with minimal RFI and days with heavy RFI were both flagged using CASA and LOFAR flagger and the results were compared. In the figure 4.3 there is a baseline shown with flagging by TFCROP+RFLAG in pink and the LOFAR flagger in yellow. While both RFLAG and TFCROP would suffice to flag all the data iteratively, there are concerns over a significant fraction of good data(up to 15 percent) being flagged out in addition to RFI an aspect that was a non issue with the LOFAR flagger, making it the best choice for our pipeline processing.

4.0.3 Calibration

The matrix for calibration for an antenna m as given by Hamaker et al. (1996), Sault et al. (1996)

$$J_m = J_{rot} J_G J_D \tag{4.1}$$

where

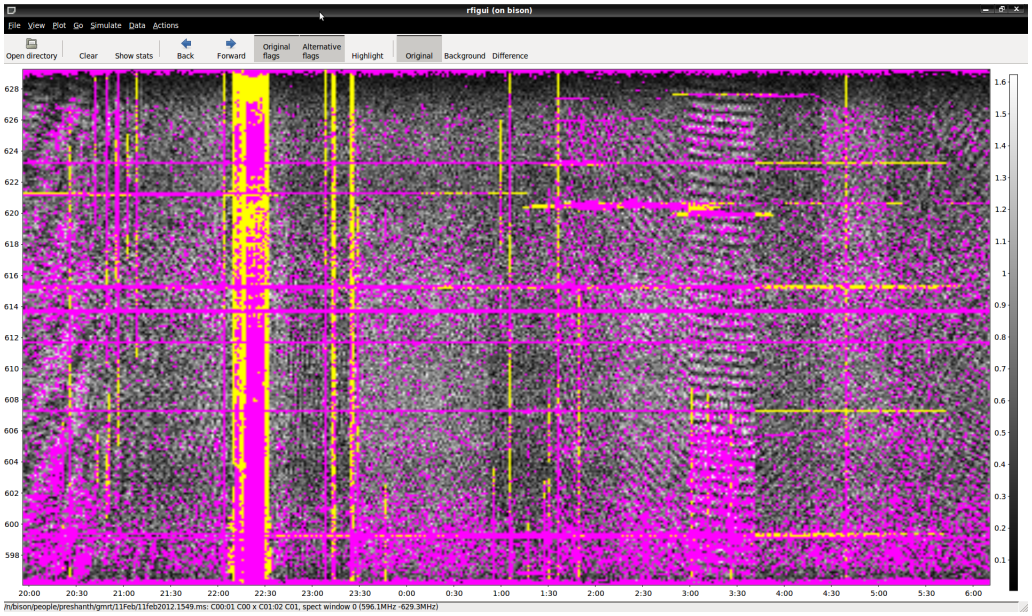

Figure 4.3: The LOFAR flagger is shown in yellow, The combined CASA flaggers in pink. Note the excess flagging of regular data by the RFLAG and TFCROP combination

$$J_{rot} = \begin{bmatrix} e^{-i\psi} & 0 \\ 0 & e^{-i\psi} \end{bmatrix} \tag{4.2}$$

ψ is the parallactic angle of the source. The parallactic angle is the measure of the rotation of the observing feeds of an alt-az antenna while tracking a source during the observation. This is an aspect unique to alt-az dishes and is not the case for equatorially mounted antennas.

$$J_G = \begin{bmatrix} g_r & 0 \\ 0 & g_l \end{bmatrix} \tag{4.3}$$

g_r is gives the gain for the right circular antenna feed and g_l gives the gain of the left circular antenna feed.

$$J_D = \begin{bmatrix} 1 & D_r \\ D_l & 1 \end{bmatrix} \tag{4.4}$$

D_r is the instrumental polarization, or the leakage of Stokes I onto of the right circular feed and D_l is the instrumental polarization of the left circular feed.

The source Stokes visibility vector can be written as

$$V_s = \begin{pmatrix} I \\ Q \\ U \\ V \end{pmatrix} \tag{4.5}$$

then the Stokes vector of the source in terms of the observed coherency vector for given baseline $p - q$ is,

$$V_{pq} = \boldsymbol{S} V_{S,pq} \tag{4.6}$$

where the associated transform for orthogonal circular feeds is the Mueller matrix S a 4x4 matrix and

$$\boldsymbol{S} = \begin{pmatrix} 1 & 0 & 0 & 1 \\ 0 & 1 & i & 0 \\ 0 & 1 & -i & 0 \\ 1 & 0 & 0 & -1 \end{pmatrix} \tag{4.7}$$

the true Stokes visibility vector to the measured coherency vector is the relation

$$V'_{pq} = (J_p \otimes J_q^*) \boldsymbol{S} V_{S,pq} \tag{4.8}$$

the coherency vector in terms of the cross hands is

$$V'_{pq} = \begin{pmatrix} V'^{RR}_{pq} \\ V'^{RL}_{pq} \\ V'^{LR}_{pq} \\ V'^{LL}_{pq} \end{pmatrix} \tag{4.9}$$

the matrices for the baseline $i-j$, the gains of the antennas i, j, the instrumental feed polarization and the parallactic angle ψ_i is

$$(J_i \otimes J_j^*)S = \begin{pmatrix} g_{rp}g_{rq}^* & g_{rp}g_{rq}^*D_{rq}^* & g_{rp}g_{rq}^*D_{rp} & g_{rp}g_{rq}^*D_{rp}D_{rq}^* \\ g_{rp}g_{lq}^*D_{lq}^* & g_{rp}g_{lq}^* & g_{rq}g_{lq}^*D_{rp}D_{lq}^* & g_{rp}g_{lq}^*D_{rp} \\ g_{lp}g_{rq}^*D_p & g_{lp}g_{rq}^*D_{lp}D_{rq}^* & g_{lp}g_{rq}^* & g_{lp}g_{rq}^*D_{rq}^* \\ g_{lp}g_{lq}^*D_{lp}D_{pq}^* & g_{lp}g_{lq}^*D_{lp} & g_{lp}g_{lq}^*D_{lq}^* & g_{lp}g_{lq}^* \end{pmatrix} \begin{pmatrix} 1 & 0 & 0 & 1 \\ 0 & -ie^{-i2\psi_i} & e^{-i2\psi_i} & 0 \\ 0 & -ie^{i2\psi_i} & -e^{i2\psi_i} & 0 \\ 1 & 0 & 0 & -1 \end{pmatrix} \tag{4.10}$$

Solving for g_r, g_l, D_l, D_r was accomplished by means of a code written in python utilizing the tasks and tools in CASA which allows us to generate the calibration tables and apply the necessary corrections. The gains $g_{r,}, g_l$ are a function of both time and frequency. The frequency dependent gain is known as the bandpass of the antenna. The computation of the leakage terms was also carried out but are second order corrections for Stokes I imaging and hence not carried out. This can be shown easily by taking the product of the two matrices in the above equation. The first term of the diagonal looks like $g_{rp}g_{rq}^*(1+D_{rp}D_{rq}^*)$. The product of the leakage terms is $<< 1$. In the coming sections the parameters of the calibration and imaging pipeline are laid out.

An explanation of the routine used for calibration and the parameter values are given below.

1. The **setjy** command in CASA was used to set the flux densities for 3C286 at 21.069 Jy. The command scales the observed fluxes with the actual flux of the calibrator that is provided as an input. As the work involved only the Stokes I intensity image the setjy value did not include other Stokes components and hence was set to zero. The command used was as follows.

   setjy(vis='11feb.ms', field = '3C286', spw = '0', scalebychan=True, flux density= [21.069,0,0,0], async = false)

2. The **bandpass** command in CASA was used to correct for the observed bandpass. We can solve for the antenna based gains using the bandpass command in order to fix the gain variations as a function of frequency. The bandpass command computes the gains of the individual antennas and obtains the form of the bandpass solutions and the required correction to remove the effect of bandpass on the calibrator given.

   bandpass(vis='11feb.ms', caltable = '11feb.bcal', field = '3C286', spw = '0', refant = '8', minblperant = 3, solnorm = true, solint = 'inf', bandtype = 'B', fillgaps = 8, append = false, parang = true, async = false)

3. The **Gaincal** command derives the complex gains g_i and θ_i as discussed in the section above. The absolute magnitude of the gain amplitude g_i are determined by reference to our standard flux density calibrator 3C286. We determine the relative gain amplitudes and phases for the different antenna using 1549_506 and compare it with those of 3C286 to then get the absolute flux density scaling. The command used was as follows..

   gaincal(vis='11feb.ms', caltable = '11feb.gcal', field = '3C286,1549+506', spw = '0:10~85', refant = '8', solint = 'inf', minblperant = 3, solnorm = false, gaintype = 'G', combine = '', calmode = 'ap', gaintable = ['11feb.bcal'], gainfield = ['3C286'], append = false, parang = true, async = false)

4. The **Fluxscale** command is used to scale the fluxes of the secondary calibrator 1549+506 based on the gains computed using gaincal. The assumption is that the gain amplitude of the primary and secondary calibrators is the same and hence knowing the flux of the primary calibrator we can then scale the secondary with reference to that. The command used was as follows.

   fluxscale(vis='11feb.ms', caltable = '11feb507.gcal', reference = ['3C286'], transfer =['1549+506'], fluxtable = '11feb.fluxscale', append = false, async = false)

5. The **Applycal** command is used to apply the computed calibration parameters

such as bandpass and gaintables onto the measurement set. The measurement set has 3 different columns : data, model and corrected. The calibration is by default applied to the corrected data column. For further processing and imaging the corrected column of data is the one that shall be used. The applycal command transfers the bandpass and fluxscale onto 1549+506 and the EN1DEEP00 fields utilizing the gains computed for both the calibrators. The command used was as follows..

applycal(vis='11feb.ms', field = '1549+506, EN1DEEP00', spw ='0', gaintable = ['11feb.bcal', '11feb.fluxscale'], gainfield =['3C286','1549+506'], parang= true, async = false)

With the visibility data calibrated and corrected for time and frequency variations we then proceed to image our data by means of the CLEAN command in CASA. The CLEAN task is named after the deconvolution process discussed in chapter 2.

4.0.4 Imaging and Self Calibration

The CLEAN image in figure 4.4 was produced using the HOGBOM clean method algorithm as implemented in CASA. At low frequencies and for long baselines like in the case of GMRT the w term in the visibility domain can not be ignored. The imaging for each pointing was done taking the w terms into account by rebinning the data using 256 bins in the w planes and then deconvolving using Hogbom CLEAN. The CLEANed image for the central field is shown in figure 4.4. With robust weighting we have been able to suppress the side-lobe structure significantly. The combined rms. noise level of each pointing is $\sim 18\mu$Jy. The pointings are subjected to self calibration as the next step in an effort to correct for the residual phase errors in the CLEANed image.

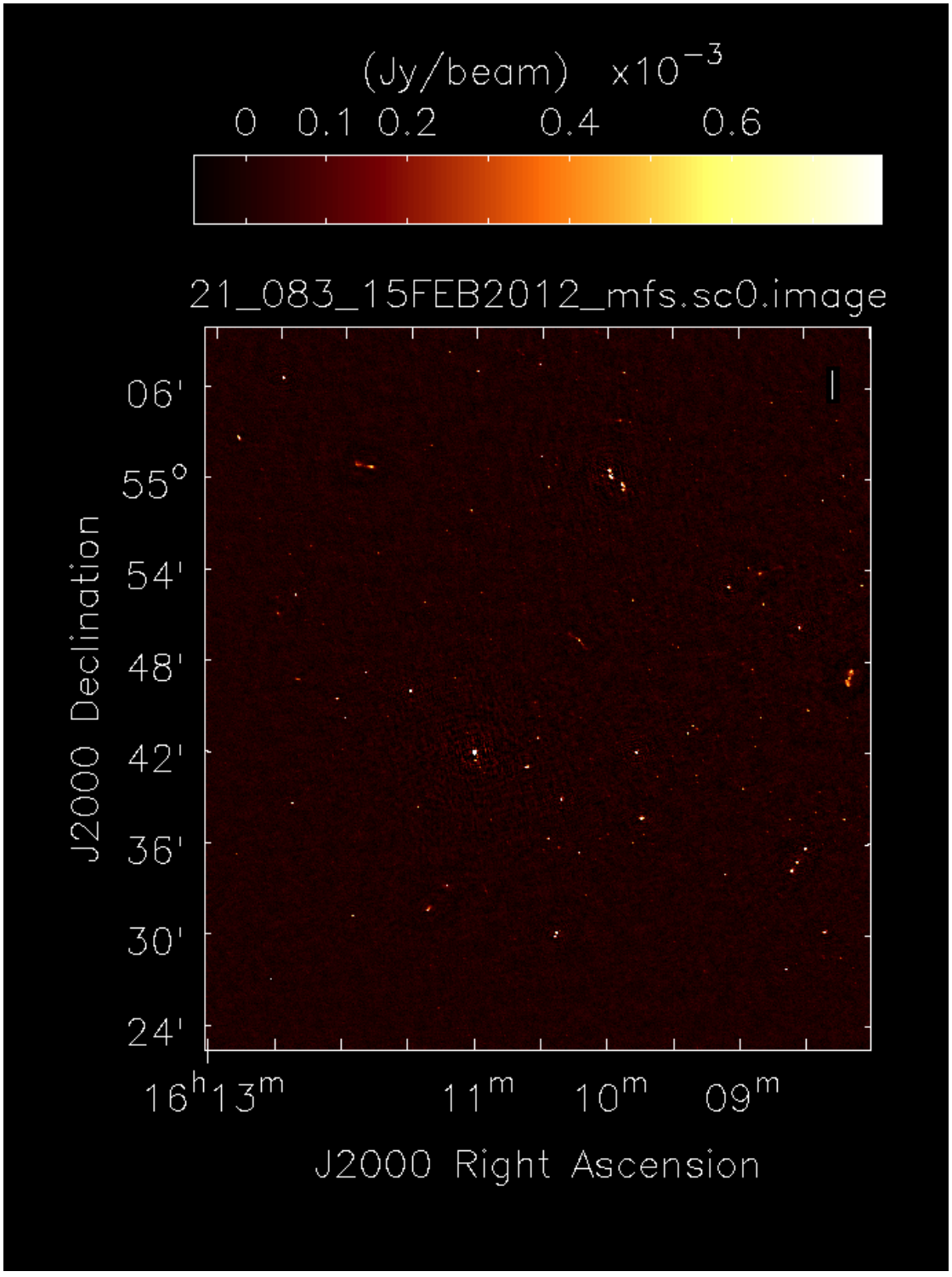

Figure 4.4: The CLEANed image field EN1DEEP 01.

4.0.5 Self Calibration

Post CLEAN there is further scope to improve the image quality of the image we produce. Given the sufficient visibility data that we have obtained it is possible to correct for the residual phase and amplitude errors in the data from running it through the pipeline. While the phase calibrators used are nearby the field there are still small phase offsets which can be dealt with iteratively with Self Calibration. A phase error of a few degrees can amount to a 5 percent change in the integrated flux measured for the sources. Correcting for the residual differential phase solutions is the role of Self Calibration.

Self Calibration uses an existing model constructed by imaging the data and uses it as a reference to compute a series of phase only gain corrections which are then applied to the data. The visibility for the i-j baseline can be modelled as,

$$V_{ij}^{'} = G_i G_j V_{ij}$$

where $G_i$is the complex gain for the i^{th}antenna and V_{ij} is the true visibility. For an array for N antennas at any given instant there are $N(N-1)/2$ visibility data and only N gain factors. In an array of antennas where $N > 8$ the solutions to the set of coupled equations can be obtained quickly. The details for the self calibration procedure are as given below.

- Produce an image, which was done in our case using the CLEAN command in CASA.
- The gains are derived by comparing the DATA column of the measurement set with the Model column which is just a Fourier transform image of the image. The corrections are stored in an external gain table and applied to the measurement set.

The process is repeated with gain solutions for decreasing time intervals computed and applied, given sufficient SNR. Given the deep field has sources of low total image flux, mustering time dependent gain solutions with a signal to noise of 10 was not possible for

solution intervals of under 2 minutes in duration. So iterations of 30, 20,15, 10, 7, 5, 3 and 2 minutes are applied one step at a time to produce a significantly improved image as a shown in figure 4.5

The self calibration reduced the noise level from $\sim 18\mu$Jy to $\sim 15\mu$Jy per pointing. The self calibrated data were then linearly mosaicked in the image domain to obtain the hexagonal mosaic. The resulting mosaic is shown in figure 4.6, and became the starting point for subsequent analysis.

4.0.6 Primary Beam - Data Processing

Knowledge of the primary beam is required to correct for off-axis errors in the final mosaic. These errors are noticeably large around strong sources that are away from the phase centres of the individual pointings. The errors in imaging are due to non circularity of the primary beam. To determine the primary beam of the antenna an observation of an 81 pointing grid around a primary calibrator was performed, with each grid-point 5 arc-minutes apart in Right Ascension and Declination around the primary flux calibrator 3C48 was carried out in March 2012. Two of the antennas were pointed at the source at all times as a reference while the other 27 working antennas of the array cycled through the grid in providing us a grid sampling the primary beam of the antennas. For a list of observation dates and reference antennas used refer to table 4.2

The calibration for the data were performed in CASA using the tasks GAINCAL and POLCAL accounting for the parallactic angle rotation. The data were initially flagged for RFI contamination using the FLAGDATA task in CASA following which antenna delay corrections were applied. The flux density of the flux calibrator was set using the SETJY task before bandpass and gain calibrations were performed. The BANDPASS and GAINCAL commands produced the bandpass and gain solutions which were then applied to compute the instrumental polarization leakage correction using 3C48 as the targeted unpolarized

calibrator source at 610MHz. POLCAL in 'Df' mode was used to obtain instrumental polarization leakage solutions per channel. The obtained calibration table solutions were applied to the data using the APPLYCAL task. To image the antenna primary beams we need to obtain the amplitude of the visibilities across the observed grid and this was done by means of a python code utilizing the CASA tbtool which lets us access and manipulate the measurement set tables.

The two reference antennas used to track 3C48 throughout the observation were W05 and C06. A quick plot of the baseline visibilities of both the antennas show that they were not functioning properly. The plot of the visibilities of a regular baseline in figure 4.7a and a plot of a reference antenna baseline in figure 4.7b are shown for comparison. We can see the raster scan show up as a change in amplitude according to the field being scanned, in the case of the reference antenna there is no regular change in the amplitudes as a function of the field of their pointing. An additional point to note is that despite normalization to unity the actual amplitudes are much lower for the reference antenna indicating that the data is spurious.

To obtain the beam, the calibrated grid visibility amplitudes were fit with a gaussian to obtain the beam shape and offsets. The RR and LL beams were obtained and then combined to produce Stokes I and V beams to which the gaussians were fit. The fits were interesting in that some of the antennas displayed more elongated elliptical beam shapes. This deviation form circularity would mean that the sensitivity is direction dependent and knowledge of the exact beam shape vital for flux corrections. The elliptical beam also implies that the sampled source flux would change as a function of the position angle of the beam in the sky and would have to be corrected for during imaging to obtain the true corrected flux. This would involve the use of an algorithm that accounts for the rotation of the primary beam during deconvolution. One such method is A-Projection which is being tested at the moment for its ability to correct for the off-axis polarization calibration which is another

instance where the beam rotation causes depolarization of $\approx 5\%$ percent.

The absence of working reference baseline in our first primary beam observation as shown in figure 4.7b necessitated further observations to proceed with the primary beam analysiss. Test time was allotted by the GMRT array operations team in February of 2013. The new observations had 3 reference antennas W01, S01 & C00, one in each of the two Y shaped arms and the other in the GMRT central square. The observations were carried out in a 17×17 grid around 3C48, but due to the test time slot being cut short observing was restricted to a 17×14 grid. The time spent on each of the pointings was 7 seconds. The first 2 second of each scan was flagged out to account for the antenna settling time and the remaining 5 seconds were analyzed based on the formalism described below.

Consider the reference baseline visibilities for V_{Rj}, where R is the reference antenna, and j is any other non-reference antenna of the array,

$$V_{Rj} = \int S(l)\sqrt{B_R(l)B_j(l)}e^{ul}dl.$$

The observed calibration source is a point source and assuming it is at the phase center we expect a constant amplitude, this is the case as $l = 0$ for the phase center which implies

$$|V_{Rj}| = S\sqrt{B_R B_j}$$

where S is the source flux density, B_r the beam of the reference antenna R and B_j is the beam of the antenna j. If the reference antenna is pointed at the calibrator source then the only change in the visibilities is due to the antenna j cycling across the grid in the sky. Then visibilities of the grid are a way of sampling the primary beam of the antenna j. Now for N reference antennas then

$$< |V_{Rj}| >= \sum_R |V_{Rj}|/N$$

where N is the number of reference antennas. This averaging over R improves the noise in

Date	Grid Size	Grid Spacing	Reference Antennas	Stokes Parameters
March 2012	9x9	5 arcmin	0,10	IQUV
February 2013	17x14	5 arcmin	0, 19, 21	IQUV

Table 4.2: Primary beam observation dates and reference antenna used.

the beam estimate by $\sqrt{N}$. To improve the accuracy, increasing the number of reference antennas is therefore recommended.

Of the three reference antennas used for the observation from Feb 2013, the reference baseline plots for C00-W01 and C00-S01 are shown in figure 4.8. Antenna W01 shows jumps in the antenna gains as a function of time. This seems to be a real effect and not a calibration problem as it was originally thought to be. The confidence in the claim stems from the fact that the same effect is not visible in the reference baseline C00-S01, and seems to arise irrespective of the choice of the reference antenna for calibration. We therefore did not use the data from W01 and the beam was computed by averaging the beam shapes from the remaining two reference antennas (C00, S01).

For an ideal on-axis calibrated antenna pair(figure 4.9) with circular feeds the cross-correlations in terms of the Stokes parameters are defined as

$$V_{RR} = I + V \tag{4.11}$$

$$V_{LL} = I - V \tag{4.12}$$

$$V_{RL} = Q + iU \tag{4.13}$$

$$V_{LR} = Q - iU \tag{4.14}$$

The above four equations were used in a python script to compute the full-Stokes beam shapes from the on-axis calibrated data using CASA tools. The beam shapes are shown in figures 4.10 and 4.11.

4.0.7 Analysis

The observation of a 17x14 grid around a primary calibrator source does not provide complete coverage of the beam. This is evidenced by the fact that the first side-lobe is visible only in the upper and lower left corners of the Stokes I beam image. The polarization beam squint is detected in the Stokes V image and is at the 3% level. Beam squint occurs when the centres of the RR beam and the LL beam are displaced. The Stokes I beam also shows deviation from the expected circular beam shape. The beam squint as well as the non circular beam shape have to be accounted for during imaging to perform the requisite corrections to obtain accurate integrated fluxes for the point source in the image as a part of CLEAN. This we plan to do using the A-Projection algorithm, which requires the measurement of (or model for) the antenna aperture illumination pattern (the Fourier transform of the primary beam pattern). The Fourier transform of just the main lobe of the antenna only gives us a single pixel in the UV domain across the antenna aperture. To be able to correct for the rotation of the non-circular primary beam, scans stretching out to well beyond the first side-lobe are required. The Stokes I beam also shows a pointing offset of around 4 arcmin which is roughly at the 10 percent level of the beam width. To ascertain the primary beam completely we have requested more observation time. While time has been granted, the observations are scheduled outside the time scale of this thesis. To ascertain the pointing errors and the shape of the main lobe, elliptical gaussians were fit and the offsets computed and the results are displayed in table 4.3.

Antenna Name	Peak Normalized to reference antenna	Offset Azimuth (arcmins)	Offset Altitude (arcmins)	FWHM Azimuth (arcmins)	FWHM Altitude (arcmins)	Ellipticity
C02	1.19	1.01	1.91	47.11	45.77	0.0284
C03	0.68	0.62	1.71	54.65	53.10	0.0283
C04	0.97	1.03	2.14	49.92	48.51	0.0282
C05	1.16	0.71	2.41	46.10	44.79	0.0284
C06	1.06	0.46	1.81	46.40	45.08	0.0284
C08	1.06	0.66	1.76	46.71	45.39	0.0282
C09	1.17	0.67	1.94	45.56	44.26	0.0285
C11	1.07	0.59	2.09	46.84	45.52	0.0281
C12	1.19	0.48	2.07	44.38	43.12	0.0283
C13	0.92	0.64	1.49	49.57	48.16	0.0284
C14	1.20	0.63	1.91	46.53	45.21	0.0283
E02	1.12	0.97	1.85	44.16	42.91	0.0283
E05	1.41	0.90	1.72	46.11	44.80	0.0284
E06	1.60	1.19	1.87	47.40	46.06	0.0282
S02	1.02	1.02	1.91	52.04	50.57	0.0282
S03	1.25	0.89	1.80	52.11	50.63	0.0284
S04	1.10	1.42	1.87	51.18	49.73	0.0283
S05	0.71	0.92	1.46	53.92	52.40	0.0281
S06	1.25	0.85	1.75	45.14	43.86	0.0283
W04	1.19	0.79	1.73	45.65	44.36	0.0283
W05	1.07	0.72	1.75	46.03	44.72	0.0284
W06	1.10	0.25	1.87	44.07	42.82	0.0283

Table 4.3: These are values for the fit to the GMRT antennas. As you can see there is a difference in the beam width in the altitude and azimuth direction.

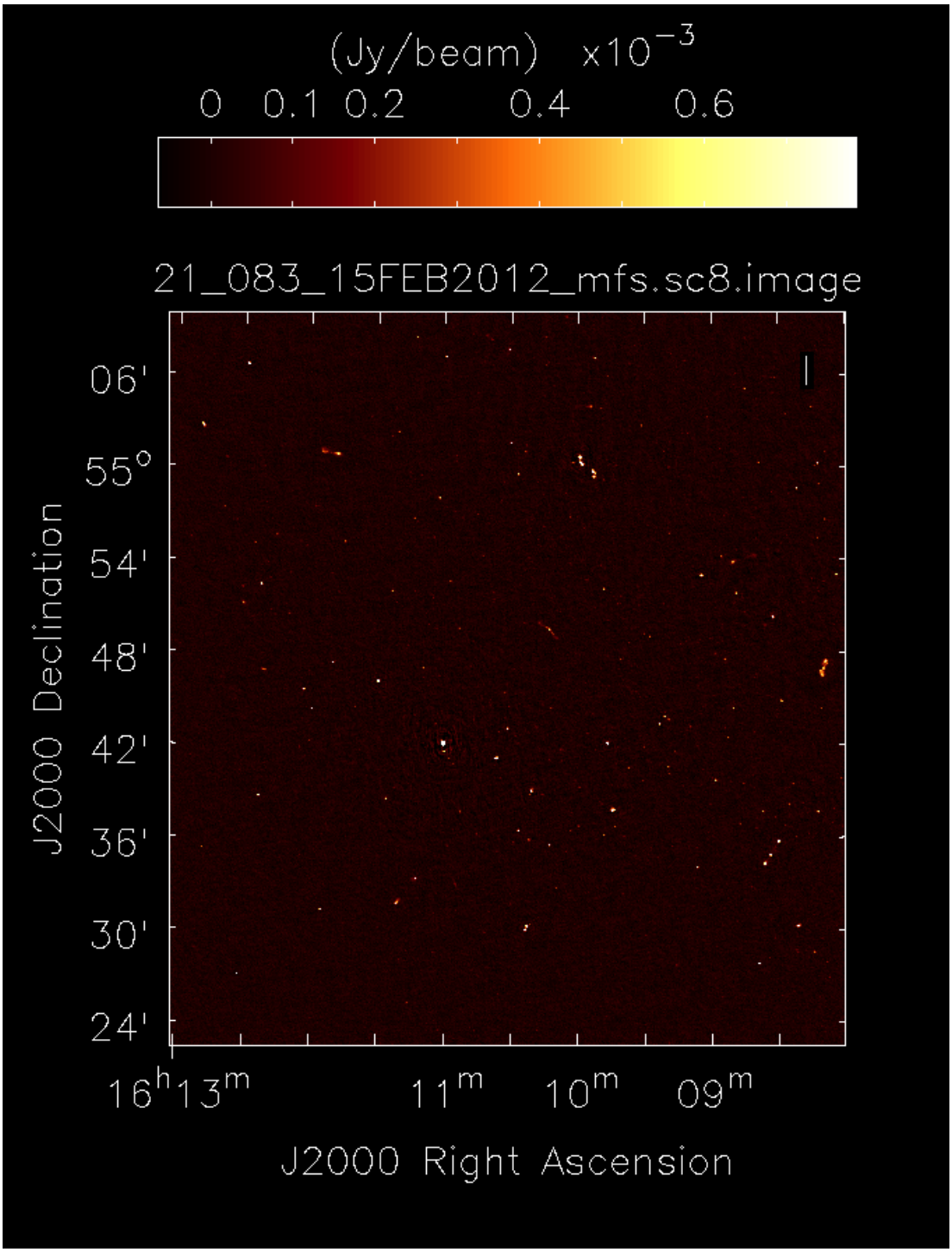

Figure 4.5: The image of field EN1DEEP 01 post selfcal. The side-lobes are suppressed.

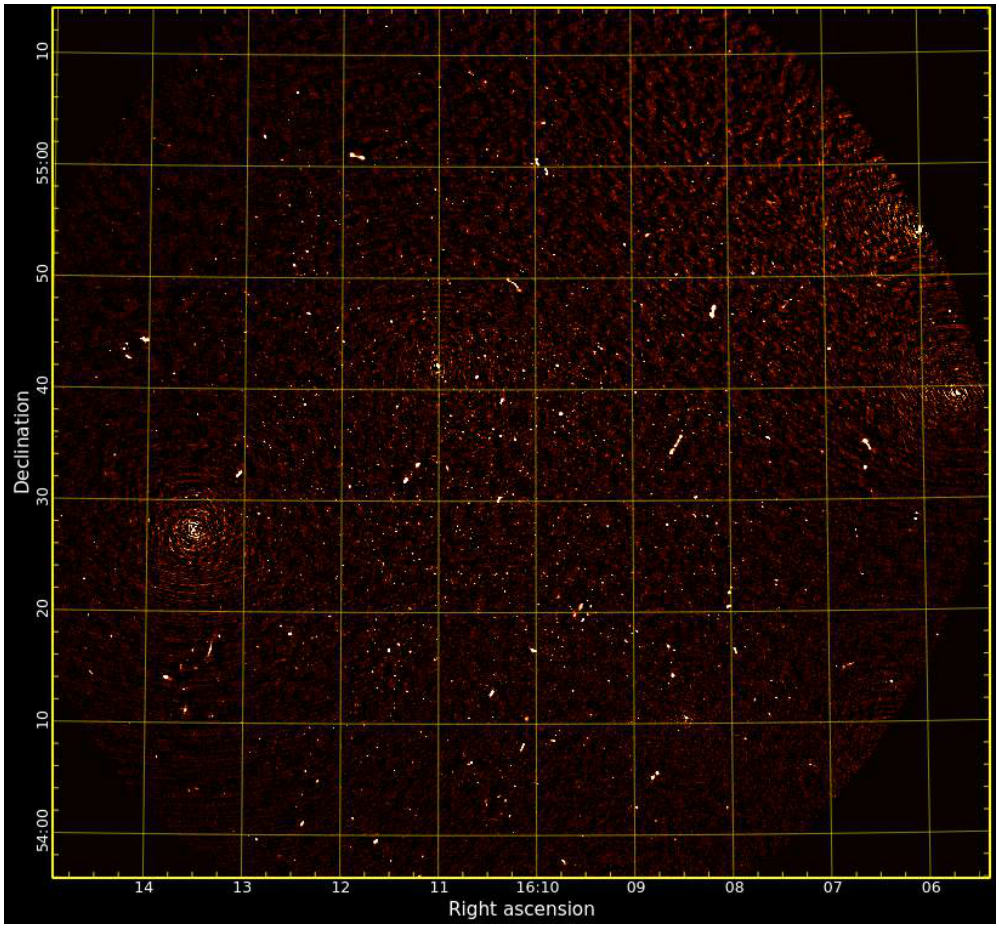

Figure 4.6: The Linear-Mosaic of all 7 pointings imaged individually with w term corrections.

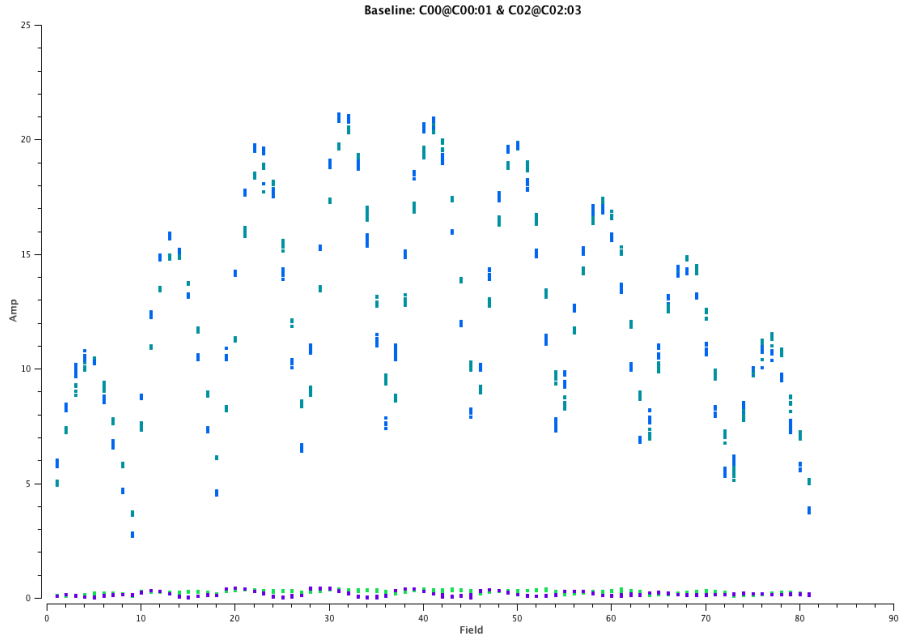

(a) Visibility amplitudes for the baseline C00 - C02.

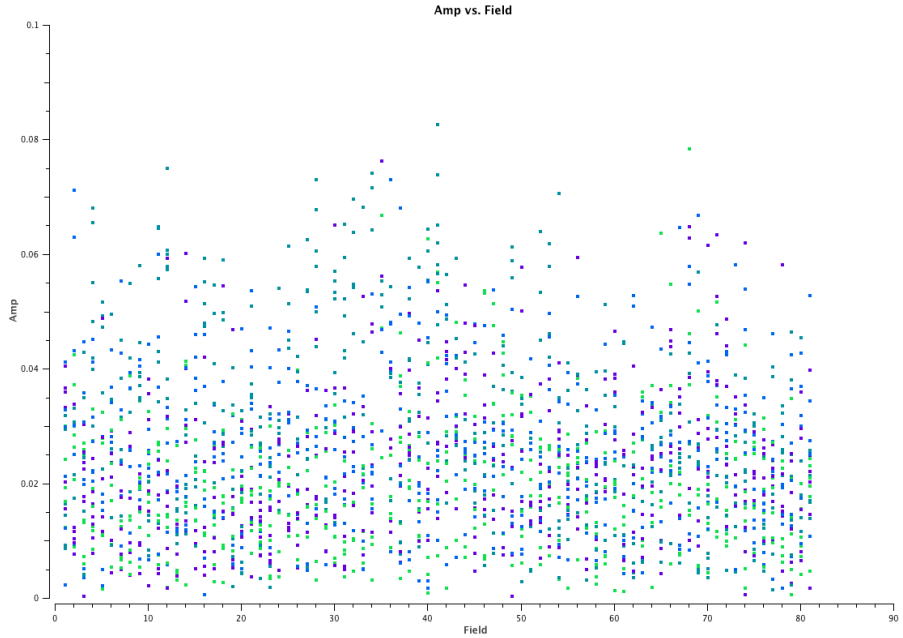

(b) Visibility amplitudes for the reference antenna C00-W05

Figure 4.7: The two figures show the clear contrast in recorded visibility amplitudes of the malfunctioning reference antenna W05 baseline when compared with what is expected from a working antenna baseline

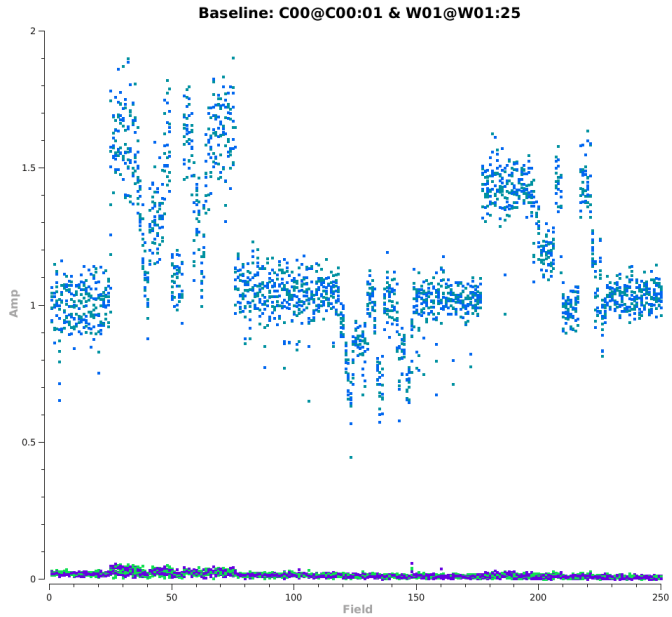

(a) Visibility amplitudes for the reference baseline C00 - C02. Plot is showing the visibility amplitudes as a function of time for all the correlations. The jumps in the amplitude caused us to drop the reference baseline from further analysis. The jumps are suspected to be instrumental gain variations and a report has been filed with the GMRT observatory accordingly.

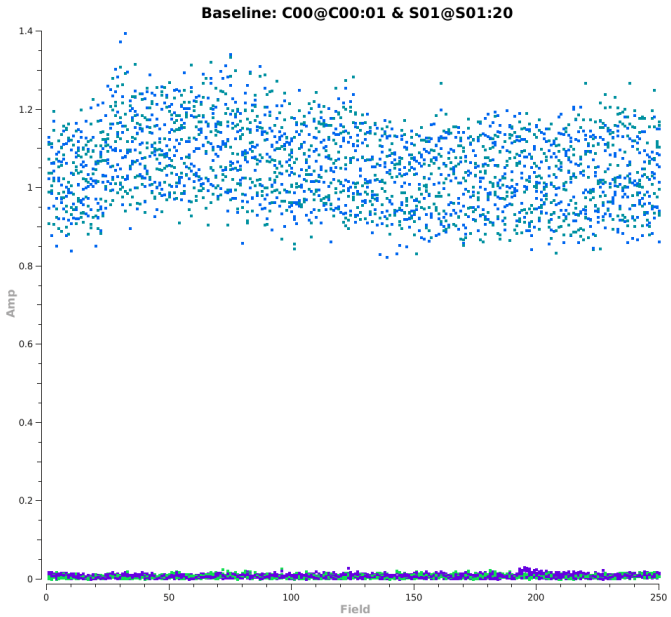

(b) Visibility amplitudes for the reference baseline C00-S01 where the visibility of the tracking reference antenna baseline is shown. If the baseline is tracking the calibrater source then there should be no change in the levels of the observed visibility amplitudes unlike in (a)

Figure 4.8: The contrast in the two reference baseline is apparent

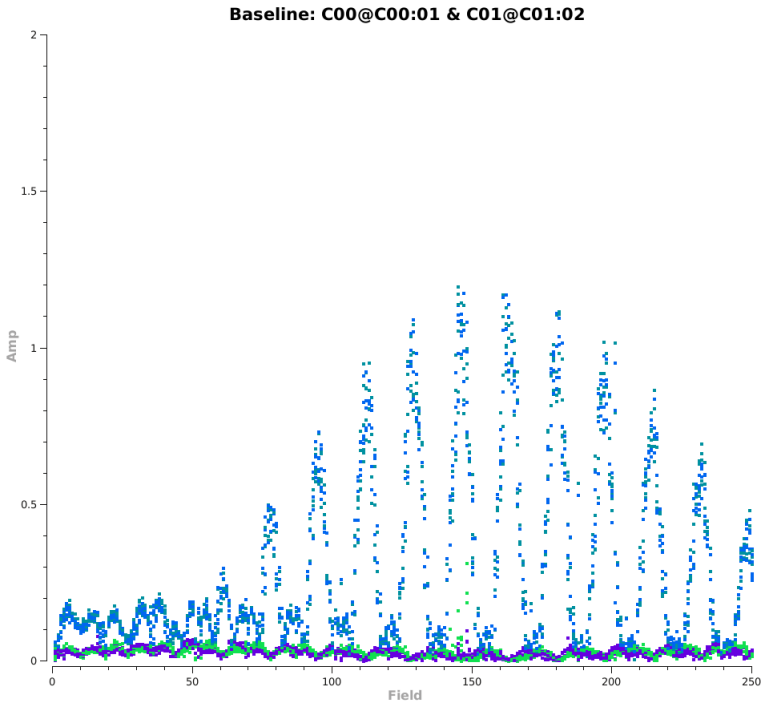

Figure 4.9: A scanning antenna C01 with a reference antenna C00 showing the amplitudes as a function of time. The four colors indicate different cross correlations dark blue and cyan showing the rr and ll, while the purple and green are rl and lr respectively. Note that from one trough to the next is a single vertical cross section across the beam.

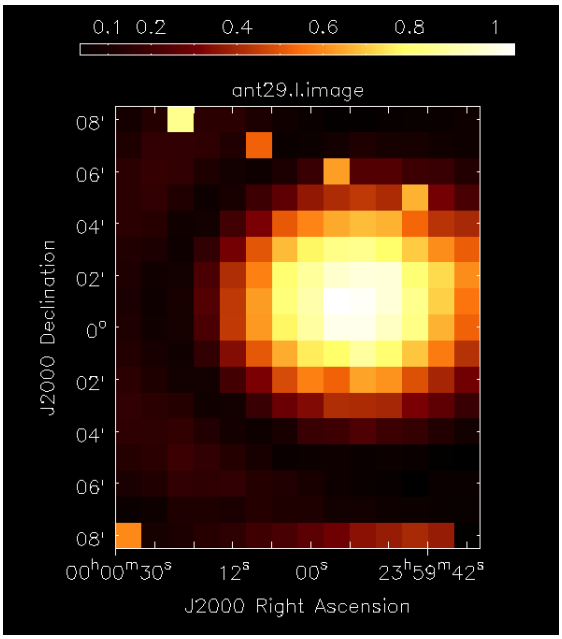

(a) The Stokes I beam shape obtained from the raster scan for antenna C01. The first side lobe is visible around the edges. The unusually high values around the edges are hot pixels to be ignored

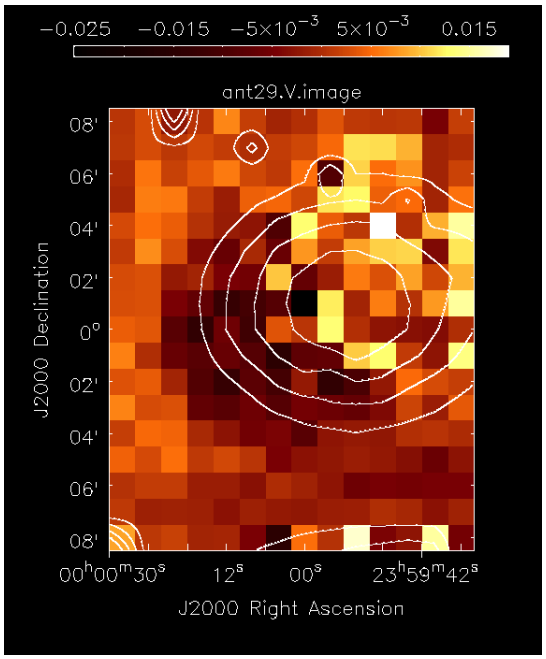

(b) The Stokes V beam of the antenna C01 showing a clear squint in the main lobe of the primary beam at the 3 % level. The white contours mark the 0.8, 0.6, 0.4, 0.2 power regions of the Stokes I beam.

Figure 4.10: The Stokes V map in (b) shows a clear dipolar disparity in the total V flux indicative of beam squint. Th elongated beam in (a) implies that rotation of a beam is an effect that has to be accounted for during deconvolution.

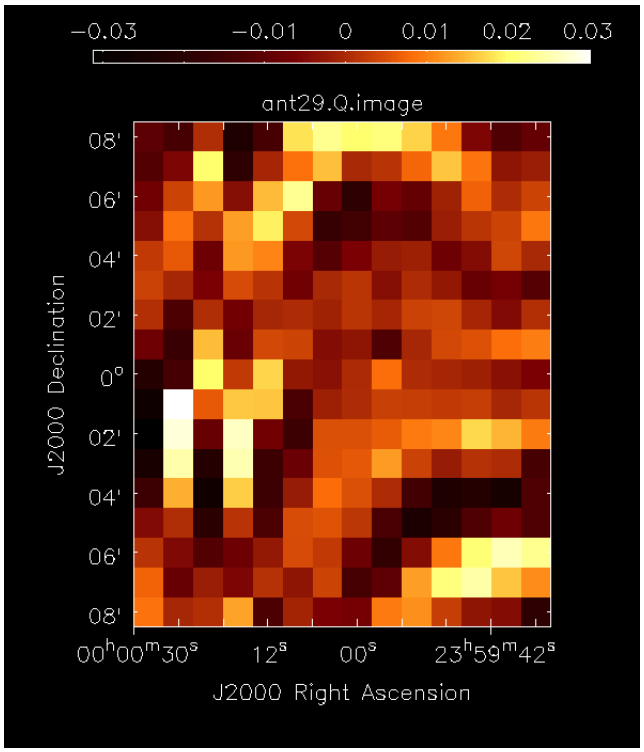

(a) The Stokes Q beam shape obtained from the raster scan of antenna C01

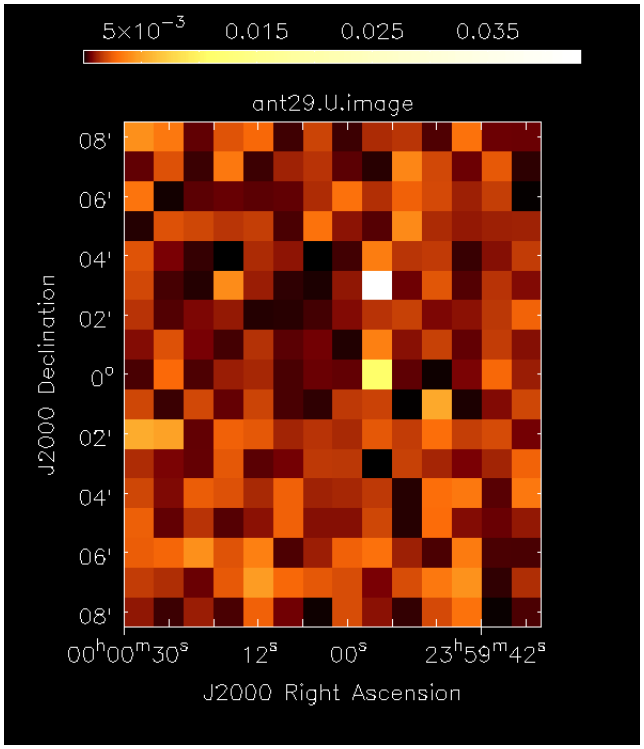

(b) The Stokes U beam shape obtained from the raster scan of antenna C01

Figure 4.11: The Beam fractional polarization while only at the 3% levels at the pointing center grows to ≈10% around the null of the Stokes I beam as clearly visible form the Stokes Q image in (a)

Chapter 5

Alignments of Radio Sources

5.0.8 Source Finding

Radio source finding on the CLEAN self calibrated image was carried out using the automated source finding algorithm AEGEAN (Hancock et al. (2012)). The source finding algorithm locates peak pixels on the map and gathers the pixels surrounding the peak pixel until the analysis threshold ($30\mu Jy$) is reached. Once the threshold is reached it then fits a gaussian to the source that has been isolated. The fit parameters are then written out to the catalog. This is repeated until there are no peak pixels left above the detection threshold. The catalogue that was produced by AEGEAN contained 1553 sources. These sources were highlighted on the image using a DS9 region file and were then perused manually to identify elongated and extended sources that had been misclassified as individual sources by the source finding software. After correct identification of separate source components as being part of a single extended source a shortlist of extended sources was obtained. In cases where only a single jet was visible the single jet was marked and the position angle of the jet obtained and included as a shortlisted source. This selection criterion led to a final sub-sample of 65 AGN jets which forms the basis of all our further analysis. From the Spitzer extragalactic representative volume survey (SERVS) the extracted AGN were matched to obtain a source corresponding to the core of the AGN jets. The matching criterion used was that the corresponding infra-red object lies within 1.6 arcsec of the radio AGN core. The 1.6 arcsec corresponds to a single pixel width in the radio image. The match yielded 48 objects of which 33 had known redshift information. The 33 object sub-sample was divided into 3 subsets depending on the object redshift (z) . The samples were classified as $z < 0.5$, $0.5 < z < 1.0$, and $z > 1$ with 12, 11 and 10 objects respectively in each sub-sample.

5.0.9 Alignments of radio galaxies

The shortlisted sources from source-finding were then analyzed to understand the underlying alignments in the radio sources. The shortlisted sources were elongated sources and are likely AGN. We derive the position angle of the jets by drawing a straight line from the centroid of the AEGEAN gaussian fit of one radio lobe to the centroid of the AEGEAN gaussian fit to the other lobe passing through the central core. The position angles are then derived from the slope of the line. Figure 5.1 shows all the sources in the field marked by the line from the peak pixel in one lobe to the other. Figure 5.2 shows all the sources in the field each with the same length line to better illustrate the position angles of the jets in the field.

5.0.9.1 Statistics on a Sphere

When dealing with position angles on a sphere, standard estimators such as the mean need to be redefined. We can clearly see that 0° and 360° are the same. Similarly the mean angle of two sources with position angles 2° and 358° is not 180°. These instances are explicitly shown to explain the need for special statistical methods for dealing with angular measures on a sphere. Fisher 1993 provides a comprehensive collection of methods of dealing with spherical statistics.

We can consider the position angles to be unit vectors on a circle in which case each angle α can be thought of as a cartesian point on the edge of the circle with coordinates $(cos\alpha, sin\alpha)$. To compute the arithmetic mean we could take the means of the cartesian points and then convert them back into polar form to obtain the mean angular measure. Given angles $\alpha_1, \alpha_2, ..., \alpha_n$ the mean is given by

$$\bar{\alpha} = arg(\frac{1}{n}\sum_{j=1}^{n} e^{i.\alpha_j}) \tag{5.1}$$

The position angle of radio sources is a random variable whose values are angles in the range$[0, 2\pi]$. The probability distribution of the positions angles of the sphere should be a uniform distribution with every angle equally likely, implying that the probability distribu-

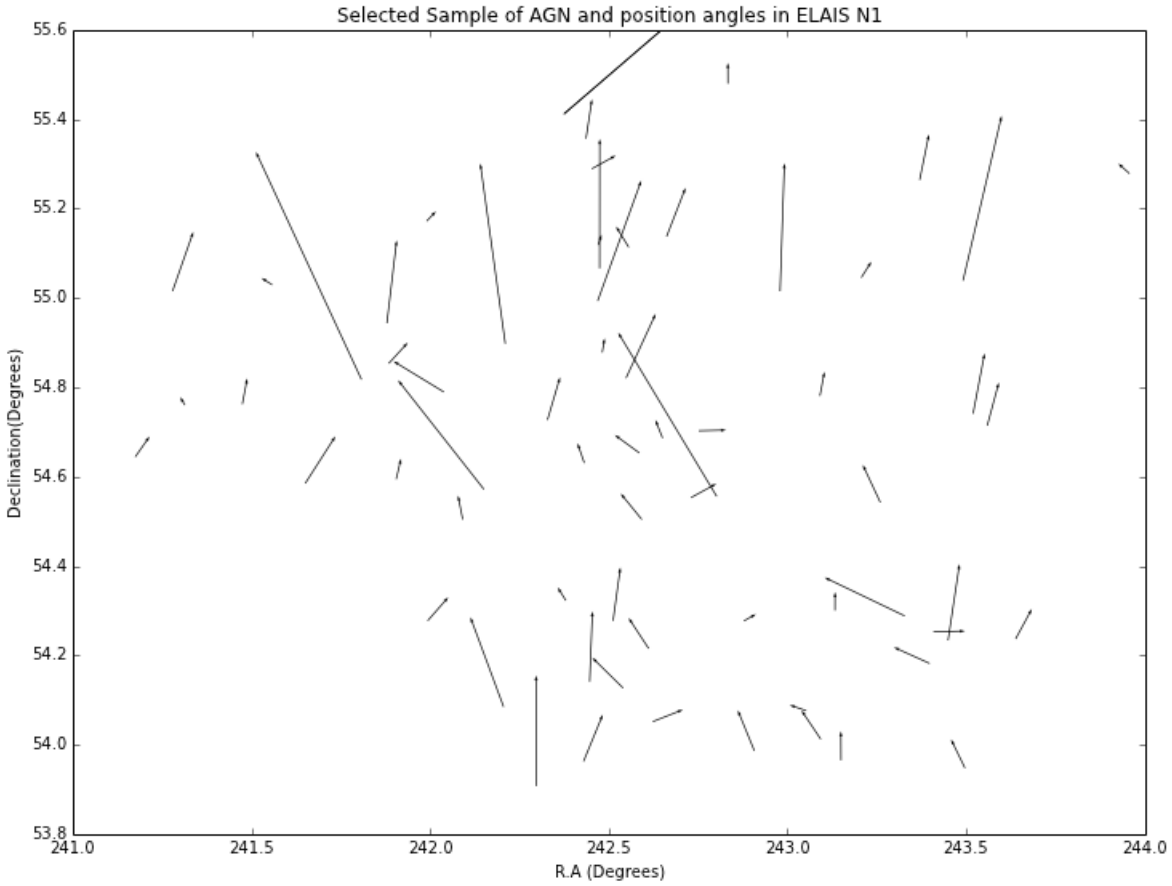

Figure 5.1: The shortlisted sources for alignment studies. The length of the line is scaled to twice the actual size of the source to show the orientations of the smaller sources.

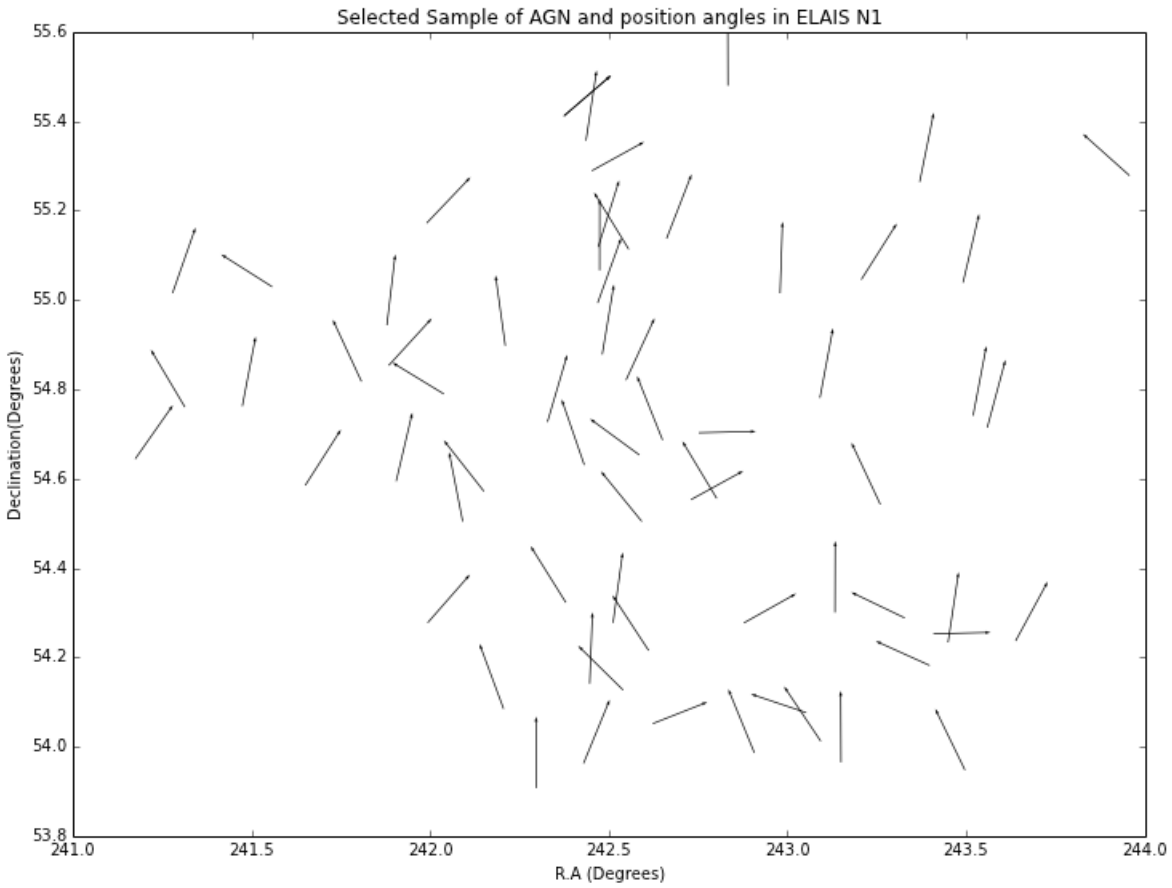

Figure 5.2: The shortlisted sources for alignment studies have been replotted here each source with the same source length. The lines of equal length helps visualize the position angles of the smaller sources more clearly.

tion function is

$$f_{UC} = \frac{1}{2\pi} \tag{5.2}$$

The moments for the uniform circular distribution are then zero. Deviations from uniformity are then testable given the circular uniform distribution function. A number of available non parametric tests are applicable to determine the level of deviation from the uniform distribution given the null hypothesis that the position angles of the jets are uniformly distributed.

The data for our tests of circular and spherical statistics and alignment is based on the reduced 65 AGN jet catalog that was selected from the catalog of extracted sources. The source catalog was utilized to compute the position angles of the AGN jets in our sample and written out as a final catalog. The catalog is then read into the statistical package R and using CircStats (Jammalamadaka and Sengupta (2001)) subpackage the circular statistical analysis on the AGN jets is carried out. The figure shows the frequency distribution of position angles.

The cosmological assumption of isotropy requires that the distribution of AGN jet position angles in the deep field be three dimensional and their orientation truly random. The position angle of the jets even in its two dimensional projection must still be random i.e. the distribution should be uniform. Figure 5.3 shows the distribution of position angles extracted. There seems to be a visually recognizable deviation from the uniform distribution.

We can test the hypothesis that the polarization angles in the final sample of 65 AGN jets are drawn from a uniform distribution using the Kuiper test as carried out by Hutsemékers (1998). We define our null hypothesis, that the distribution of measured position angles in the sky is uniform. The test statistic, V for the Kuiper test is defined as follows. Let F be the continuous distribution function which is our null hypothesis. The sample of data are independent realizations of the random variables, having F as their distribution function,

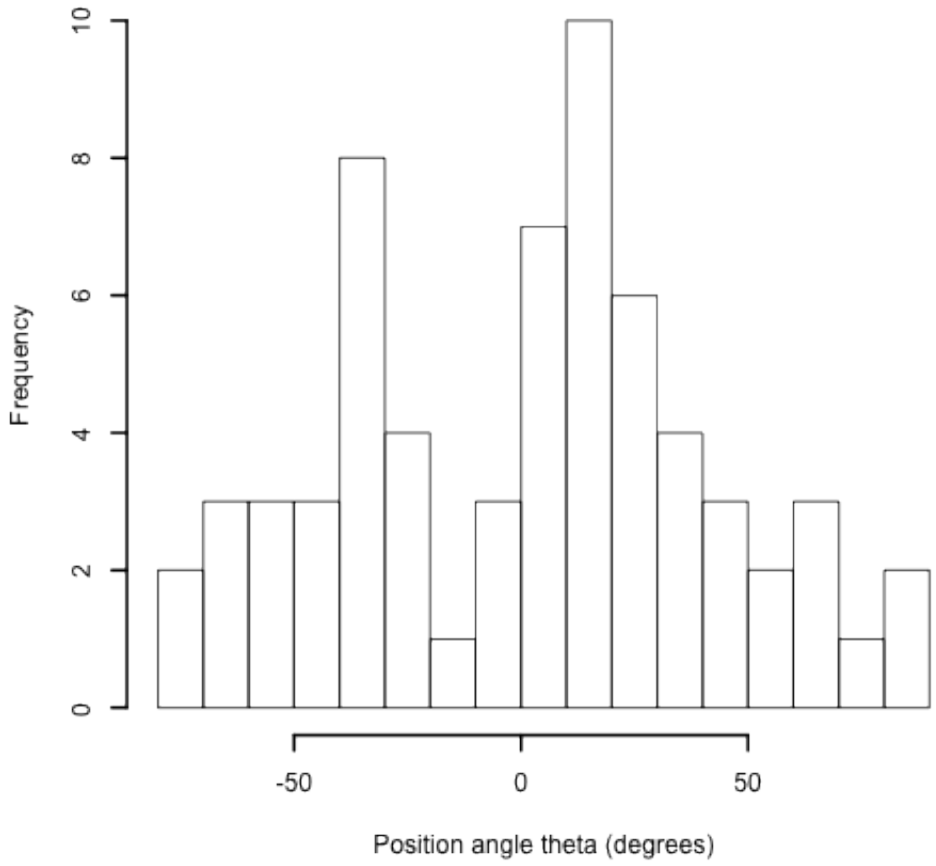

Figure 5.3: The probability distribution function of AGN jet position angles

by $x_i (i = 1, ..., n)$. Then we can define

$$z_i = F(x_i) \tag{5.3}$$

where z_i is the observed position angle.

$$D^+ = max[\frac{i}{n} - z_i] \tag{5.4}$$

$$D^- = max[z_i - \frac{i-1}{n}] \tag{5.5}$$

where D^+ and D^- are the maximum and minimum deviations respectively. The test statistic V in terms of the deviations is

$$V = D^+ + D^-. \tag{5.6}$$

The Kuiper Statistic and the significance tables (Snec (1974)) are a part of the CircStats package in R which was used for the computation of the Kuiper test. The value of the Kuiper and the Watson U^2 statistic is a function of the sample size, so for a larger sample a the test statistic a larger value of the statistic is required to reject the null hypothesis with the same level of confidence when compared to a smaller sample size.

The Kuiper test statistic of 4.5899 corresponds to $p < 0.01$. The p value is a measure of probability that the null hypothesis is valid. So a $p < 0.01$ implies a 99% confidence rejection of the null hypothesis of uniform distribution. The Watson's U^2 test for Circular uniformity was carried out to compare the results against the Kuiper test, where Kuiper uses the maximum deviation values D^+ and D^- , Watson's test uses the mean square deviation. The Watson's U^2 test provided a test statistic of 2626.54 which corresponds to $p < 0.01$ which implies a 99% significance level of rejection of the uniform distribution. The sub-sample tests and significances are shown in table 5.1.The sub-samples all reject the null hypothesis to 99% significance that the position angles in the redshift range are uniformly distributed.

Sub-Sample	Watson U^2 Statistic	Watson p-value	Kuiper Statistic	Kuiper p-value
$z < 0.5$	0.4179	$p < 0.01$	2.4604	$p < 0.01$
$0.5 < z < 1.0$	0.339	$p < 0.01$	2.1733	$p < 0.01$
$z > 1.0$	0.4395	$p < 0.01$	2.3983	$p < 0.01$

Table 5.1: The Watson and Kuiper Test for the subsamples. The sub-samples all reject the null hypothesis to 99% significance that the position angles in the redshift range are uniformly distributed.

5.0.9.2 Spatial Covariance of Position Angles

If the angles are not uniformly distributed then a measure of how they are changing as a function of angular separation is of interest. One such measure is the spatial covariance function or the variogram. In spatial statistics the theoretical variogram is a function describing the degree of spatial dependence of a random field. The variogram is defined as

$$\gamma(d) = \frac{1}{2m(d)} \sum_{j=1}^{m(d)} [z(x_j) - z(x_j + d)]^2 \tag{5.7}$$

Here the sum is over $m(d)$ pairs of points which are at a distance d from each other and z is the variable being measured at vector location x_j. In the case of stationary and isotropic spatial process the variogram reduces to a spatial covariance function

$$V(d) = \sigma^2[1 - \rho(d)]/2 \tag{5.8}$$

$$\gamma(d) = \frac{Var[V(x+h) - V(x)]}{\sigma^2} \tag{5.9}$$

where d is the distance separating the points x_i, x_j in space and σ^2 is the variance of the process S. If the distribution of the position angles of the jets were uniform, then the variogram which measures the variance of one position angle with another as a function of their separation should be uniform at all angular scales. To derive the mean variance of the uniform distribution at the locations of the AGN jets in our field a Monte Carlo simulation was carried out. The Monte Carlo simulation drew a random position angle for each of the spatial positions of the AGN jets, such that every position angle was equally

likely. Ten thousand iterations of the simulation was fit with a straight line to obtain the mean spatial variance of the data for a uniform distribution This is shown as the dotted line in the variogram. So the points not lying on the line are deviating from the truly random which indicative of alignments or anti-alignments in the jets position angles. This analysis was carried out in R using the geoR(Jr and Diggle (2001) and Diggle and Jr (2007)) tools.

The figure 5.4 shows the variogram obtained for the complete sample of AGN. Of particular interest are the points corresponding to an angular separation of 1.2°- 2.0°. Note that the points that are lying under the mean value of variance represented by the dashed line indicate low variance. Low variance implies that most sources on that angular scale bin are aligned. High variance can be thought of as an anti-alignment signal. One situation that gives rise to anti-alingment is the presence of two distinct populations. While the populations are aligned within themselves they might be anti-aligned when compared with the other population.T he other noticeable pattern is the cyclicity in the variogram. While the cyclicity could suggest that the underlying mechanism causing the alignment is periodic it has to be taken with a pinch of salt as it could just be a feature of the data.

Variograms of the different sub-samples of data can be found in figures 5.5, 5.6, 5.7. While the sub-sample containing source at $z < 0.5$ shows strong alignment signal at 0.8 degrees, the sub-sample of $z > 1.0$ also shows strong alignment signal for spatial scales from 0.4°- 1.2°.

The redshift sub-samples are all indicative of strong alignment signal. These results are indicative at best in that the sample size for the analysis is significantly reduced and along with it our confidence in them. What it does demonstrate is that the variogram is an excellent to probe to understand the global scales of position angle alignments. Having seen evidence for position angle alignments we can then compare it with the spatial clustering of AGN jets. If the scales of alignment mirror each other then we can conclude that there might be a common cause for the observed angular and spatial clustering signal. The absence of

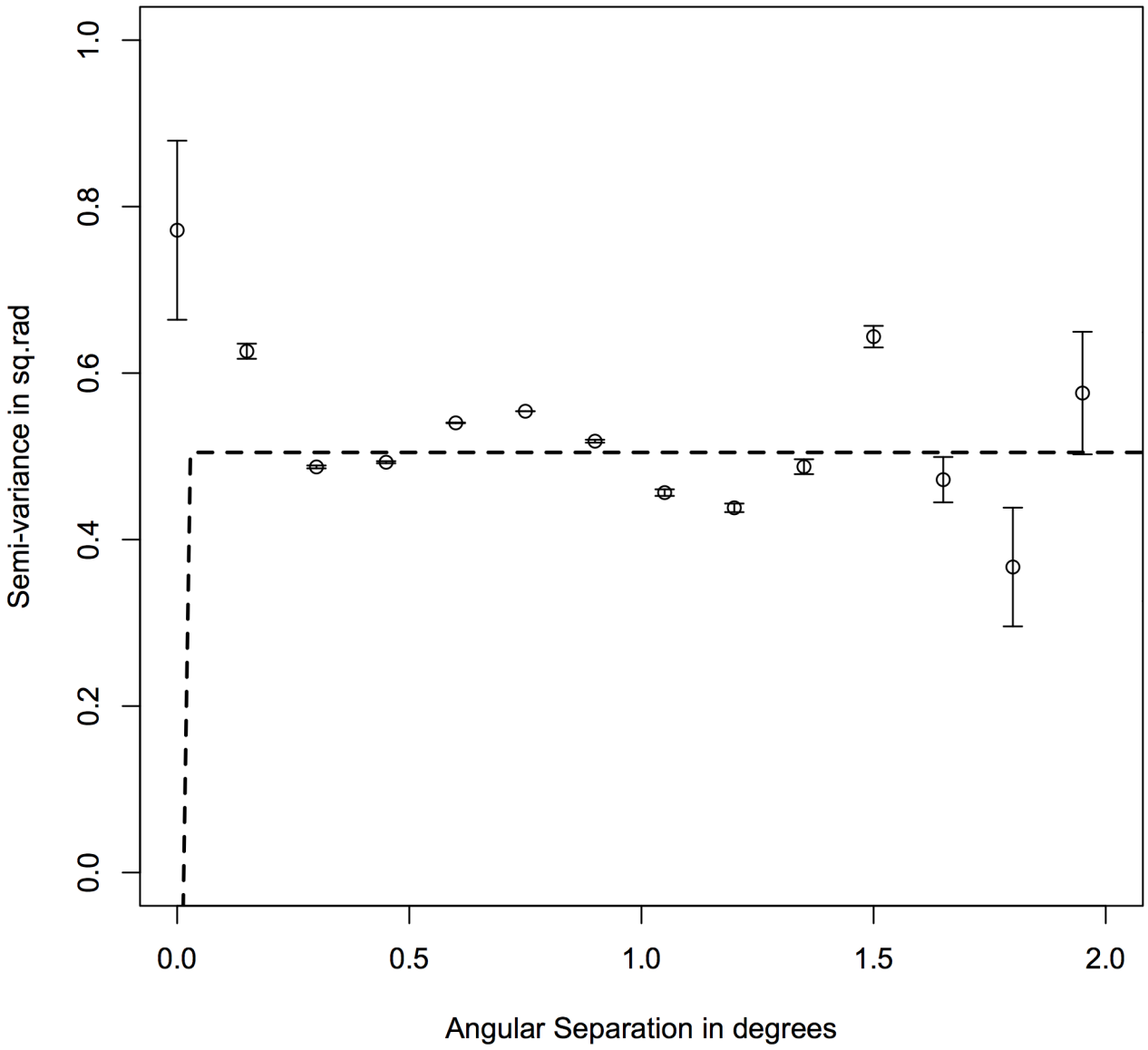

Figure 5.4: Variogram and the best fit line for the Monte Carlo simulations for the complete AGN sample. Plotted is the spatial covariance of the position angles in sq.rad as a function of the angular separation in degrees. The points lying below the fit indicate that the spatial variance is lower than the mean variance for uniform distribution which is indicative of alignments in those angular scales.

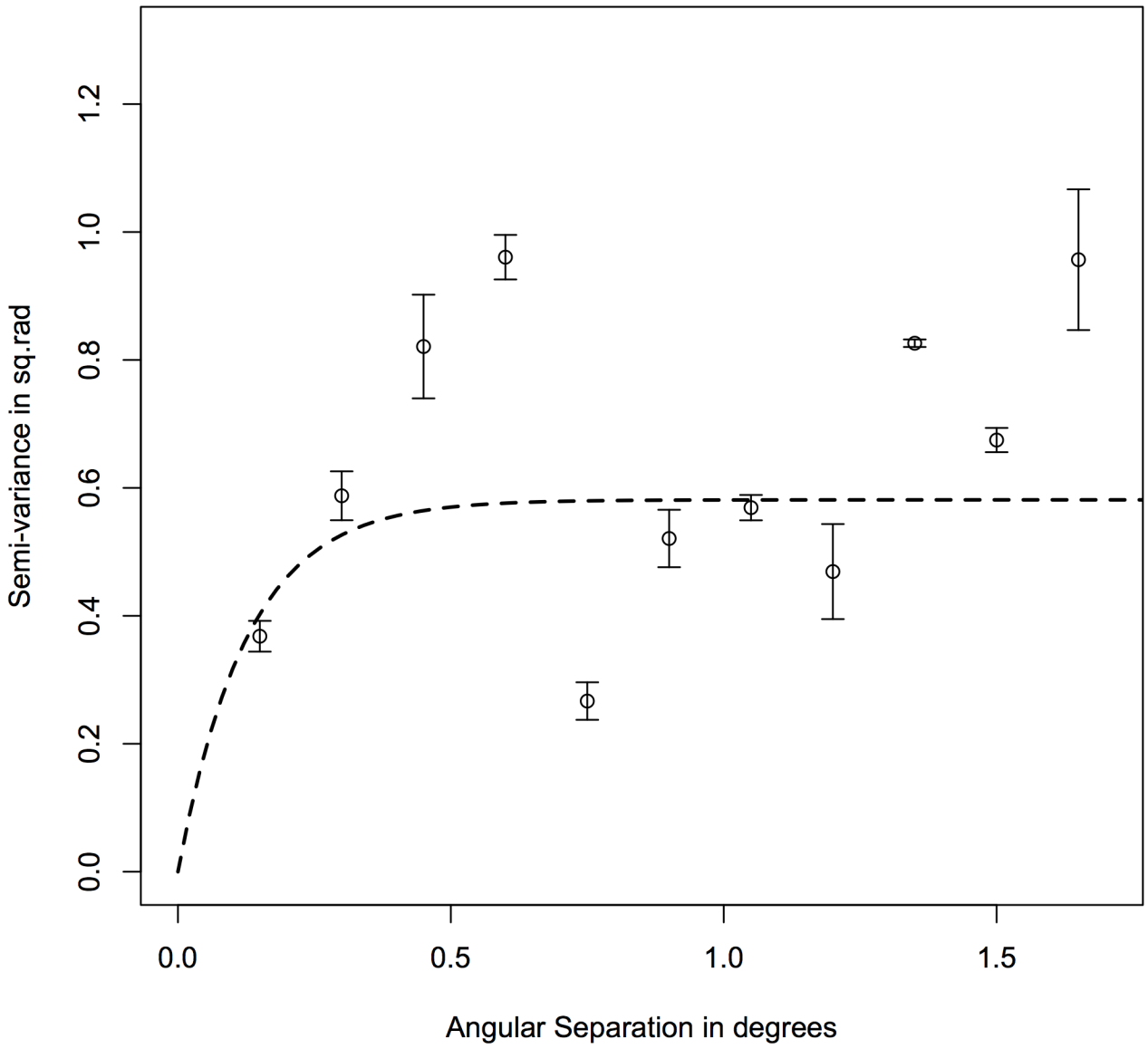

Figure 5.5: Variogram and the best fit line for the Monte Carlo simulations for the sub-sample $z < 0.5$. Plotted is the spatial covariance in rad^2 as a function of the angular separation in degrees.

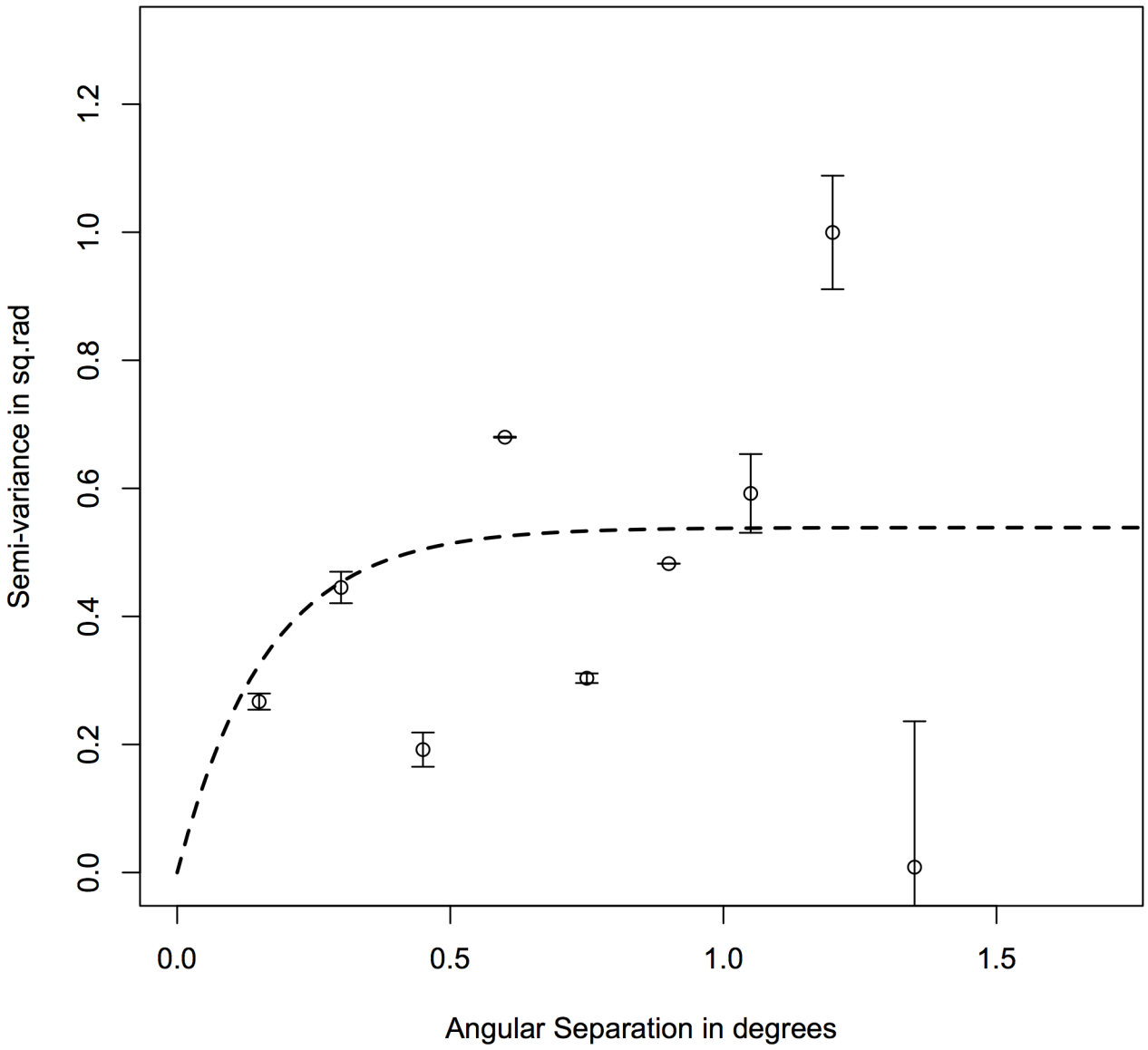

Figure 5.6: Variogram and the best fit line for the Monte Carlo simulations for the sub-sample $0.5 < z < 1.0$. Plotted is the spatial covariance in rad^2 as a function of the angular separation in degrees.

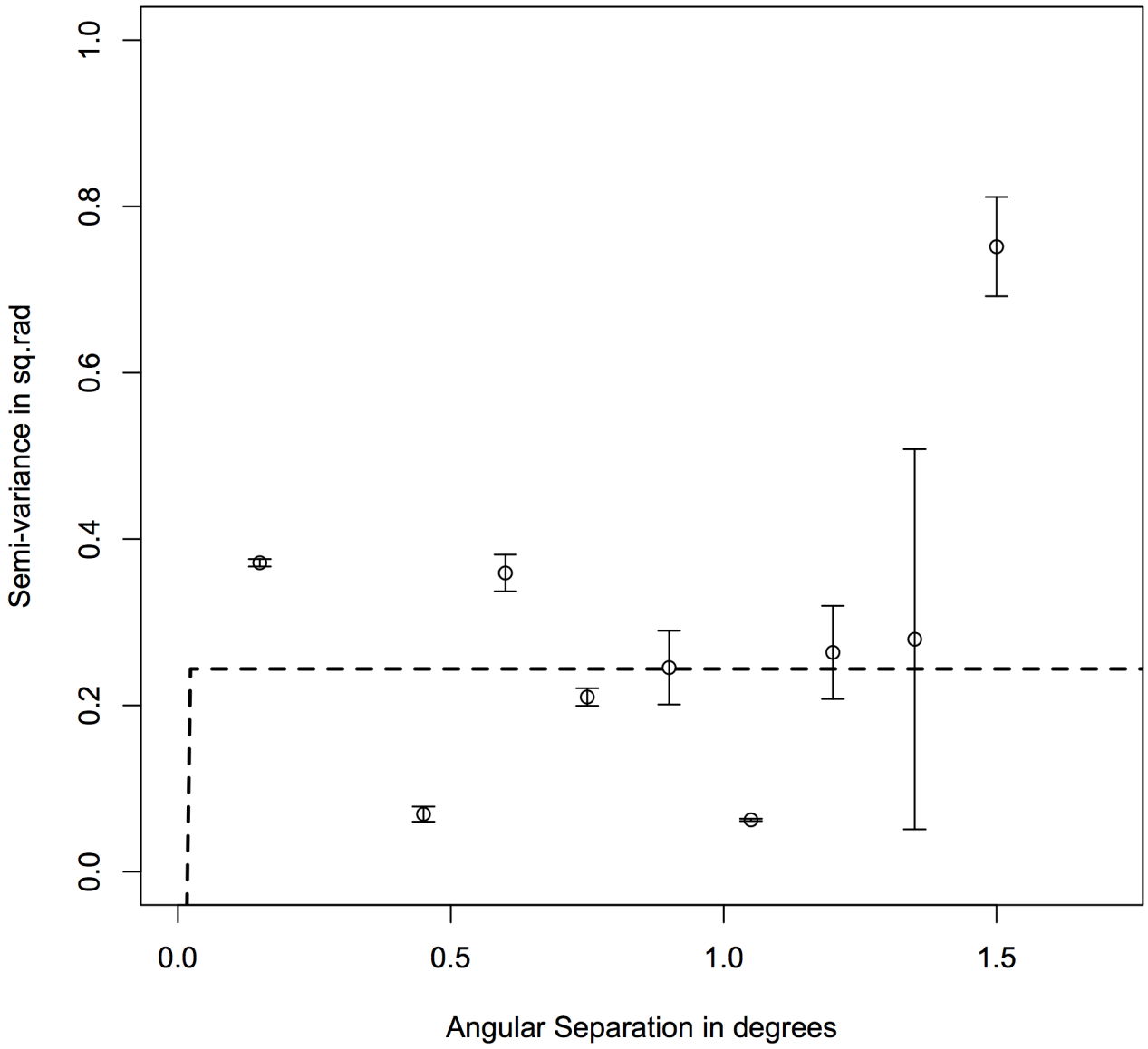

Figure 5.7: Variogram and the best fit line for the Monte Carlo simulations for the sub-sample $z > 1.0$. Plotted is the spatial covariance in rad^2 as a function of the angular separation in degrees.

correlation between spatial clustering of sources and the position angle alignment then raises the question as to the cause of position angle alignments.

5.0.9.3 Spatial Clustering of AGN Jets

The distribution of the jets is an irregular pattern of points in a 2-dimensional space on the sky. The statistical methods encompassing them are known as spatial point processes. Since the properties that we are interested in are statistically invariant under translation and rotation we can consider the processes to be stationary and isotropic. The underlying statistics of the radio jets positions is a Poissonian point process (Neyman and Scott (1958) and Martinez and Saar (2010). Since we do not know if our AGN jets are clustered we shall assume complete spatial randomness (CSR). Then the estimated distribution function $G(r)$ can be constructed and compared with the CSR expectations. For large n and ignoring edge effects the CSR distribution in a 2-dimensional area A containing n points is

$$G(r) = 1 - e^{-\pi n r^2/A} \tag{5.10}$$

The distributions of F and G functions are identical for Poissonian point processes. The Ripley's K function is another estimator of point processes and for a Poissonian point process is

$$K(r) = \pi r^2 \tag{5.11}$$

All other estimators are then defined in terms of F, G and K functions. Van Lieshout - Baddeley J function compares the inter-event distances G to distance from a fixed point F. The function is defined as

$$J(r) = \frac{1 - G(r)}{1 - F(r)} \tag{5.12}$$

$J(r)$ has been shown to be resistant to edge effects while still being very sensitive to the clustering signal (van Lieshout and Baddeley (1996)). Note that J is a ratio of two functions and for CSR $J(r) = 1$ for all r. Values of $J(r) < 1$ are indicative of clustering while values

of $J(r) > 1$ are indicative of spatial repulsion or a lattice like structure. The jet locations were supplied and the Lieshout - Baddeley j function was computed and the plot is shown in figure 5.8. The function shows a dip in the function on spatial scales of 0.075°- 0.15°, which corresponds to an angular scale of 5 arcmin to 9 arcmins. The dot dashed line shows the clustering signal for a complete spatially random process. So

The two-point correlation function has been the favorite of astronomers since the seminal works of Totsuji and Kihara (1969) and Peebles (1973). The two-point correlation function counts the number of objects in annuli around each point rather than counts within circles around each point, and hence is related to the differential of the K function (Illian et al. (2008)). The best estimator for the two point correlation function accounting for edge effects(Wall and Jenkins (2012), Feigelson and Jogesh Babu (2012)) is given by the Landy-Szalay estimator

$$\hat{\xi}_{LS} = 1 + \left(\frac{n_{CSR}}{n}\right)^2 \frac{DD(d)}{RR(d)} - 2\frac{n_{CSR}}{n}\frac{DR(d)}{RR(d)} \tag{5.13}$$

where $DR(d)$ is the number of pairs between the observed and simulated CSR distributions in the $(d, d + \Delta d)$ annulus. $DD(d)$ is the number of point pairs around the observed data points as a function of distance d. $RR(d)$ is the number of point pairs around the simulated data points as a function of d. $n_{CSR} \gg n$ where n_{CSR} is the number of simulated data points and n is the number of observed data points. As mentioned earlier

$$\xi(D) = \frac{K^{'}(d)}{2\pi d} + 1 \tag{5.14}$$

for a 2-dimensional spatial distribution(Illian et al. (2008)). The integration of the edge corrected estimator brings in the corrections suggested by Landy and Szalay (1993). This is the methodology implemented in R for the spatstat package(Baddeley and Turner (2005)) which was used to determine the Ripley's K function and the two point correlation function, shown in figures 5.9 and 5.10.

The results from the K function and the two-point correlation function identify scales of spatial correlation to be 5 - 24 arcmins, which corresponds to comoving scales of $3.06h^{-1}$Mpc

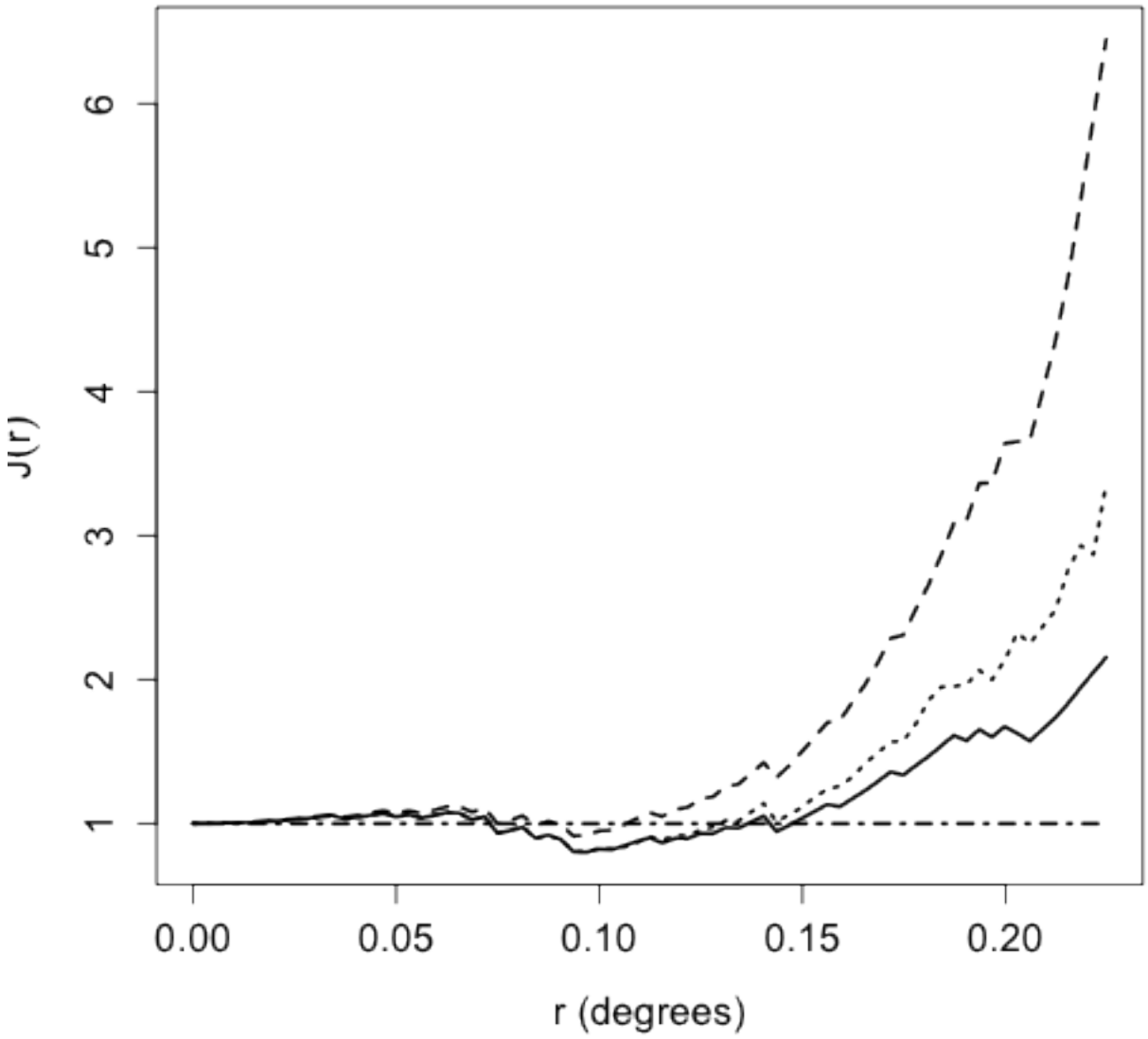

Figure 5.8: Lieshout - Baddeley J function . The dot-dashed line represents CSR. The dashed line is the estimator not accounting for edge effects. The dotted line is the estimate based on reduced number of sources to account for edge effects. The solid line is the isotropic edge effect correction.The function shows a clustering signal in the range of 0.075 - 0.15 degrees, which corresponds to an angular scale of 4.5 arcmin to 9 arcmins.

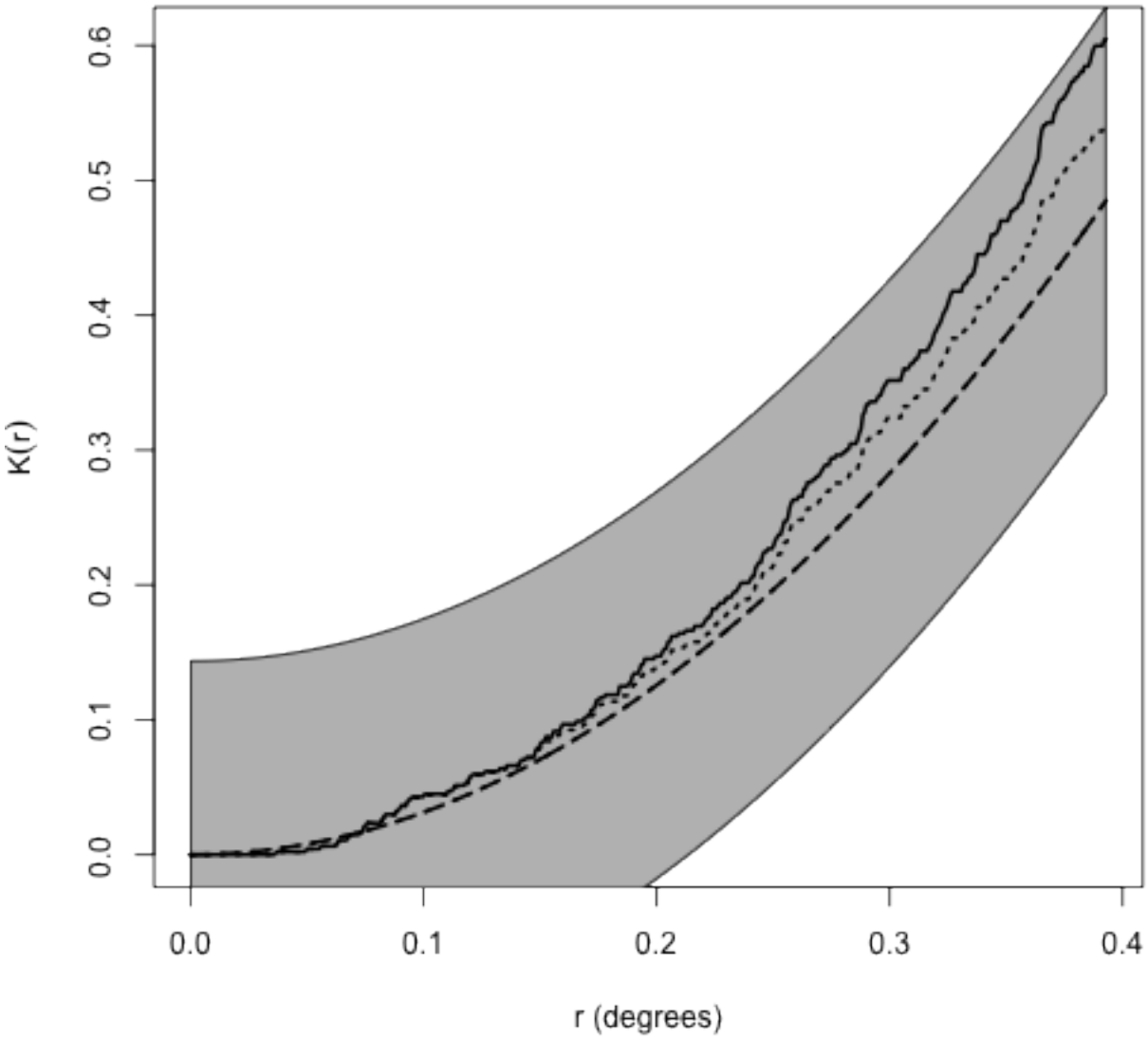

Figure 5.9: Ripley's K function. The grey band denotes the spread of values of $n_{CSR} = 10000$ simulated runs of the data. The dashed line denotes a theoretical value of a Poissonian point process. The dotted line is the estimator without edge effects. The solid line is the estimator including edge effects. Points that lie outside the grey band are deviating from Poissonian distribution distribution to 99.999% significance.

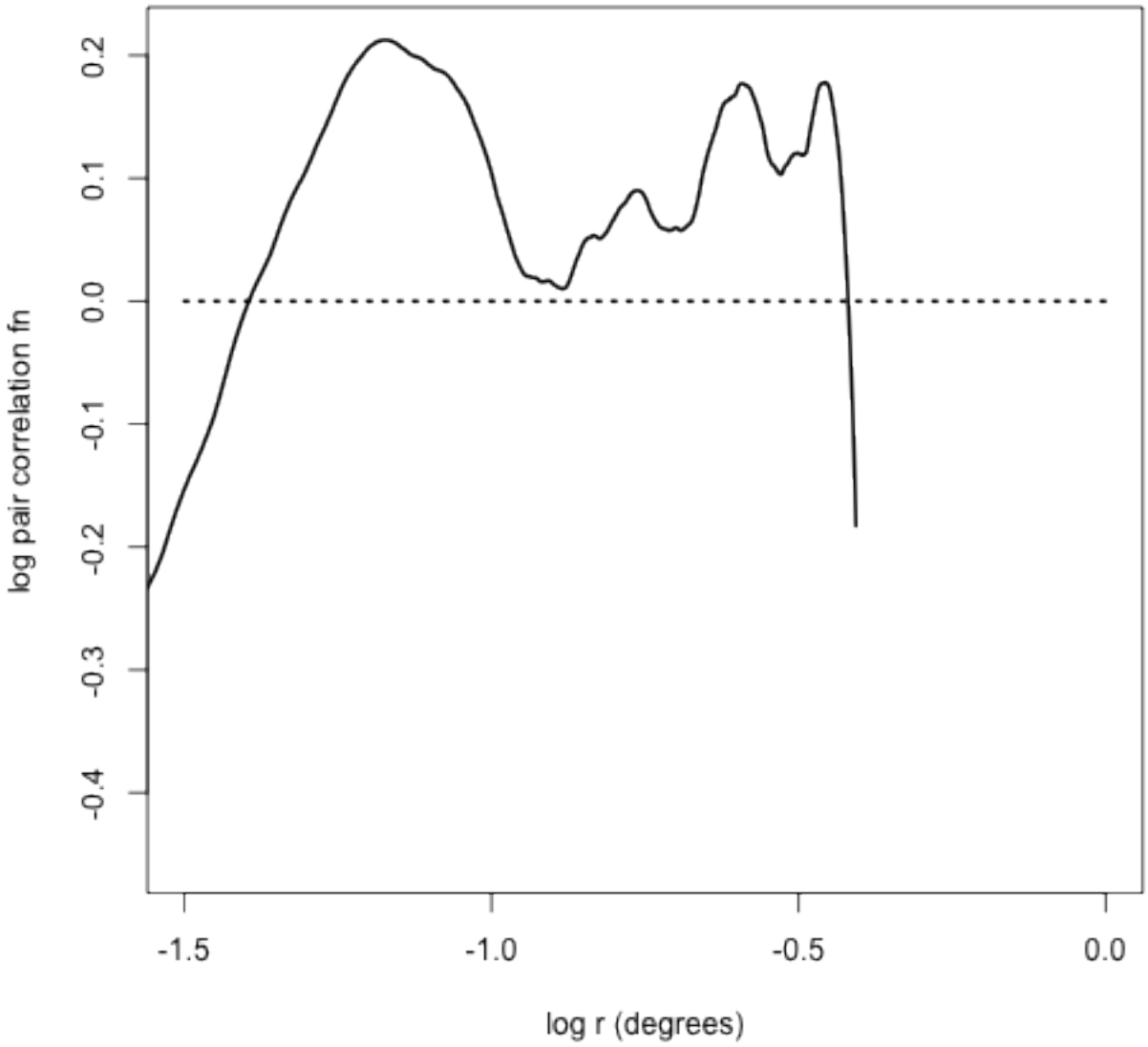

Figure 5.10: Two-point correlation function.The dotted line is the theoretical two-point correlation function assuming CSR. The solid line is the estimated two-point correlation with edge correction. The rise following the initial dip in the curve around 1.0(5 arcmin) shows that the magnitude of the of spatial correlation increases and continues to do so until spatial scales of -0.4(24 arcmin).

- 16.35h^{-1}Mpc at a redshift of ($z = 1$). These scales while matching the J function at the smallest scales extend beyond the maximum predicted by the J function of 9 arcmin.

The correlation scales of jet position angles as determined by the angular covariance function(variogram) extends beyond the scales probed by the spatial correlation function. Position angle correlation at scales of 1.2°to 1.8°translates to a comoving scale of 50-75h^{-1}Mpc at $z = 1$, scales typically larger than galaxy clusters, the largest gravitationally bound structures in the universe. The spatial correlations are restricted at the maximum to scales of 5 - 24 arcmins corresponding to 3.36 -16.12h^{-1}Mpc which are typically on the scales of galaxy clusters.

Spatial clustering has revealed the possible presence of galaxy clusters in the ELAIS N1 field as shown by Kim et al. (2011) in infrared. While the scales of AGN jet position angle alignments are larger than the largest gravitationally bound scales begs the question as to what caused them ? The AGN jet position angles could be indicative of large scale forces other than gravity that affected their formation, such as cosmic magnetic fields. It could also be residual angular momentum alignments of the central super massive black-holes that are remnants of galaxy formation that are thought to trace the filamentary structure on large scales.

Chapter 6

Conclusions and Future Work

6.0.10 Conclusion

The ELAIS N1 survey was carried out with the GMRT and a linear mosaicked W-projection corrected image was produced. The GMRT primary beam was measured out to the first side lobe. Measurements of the beam suggest that the beam shapes are elongated, which makes corrections during deconvolution vital for further deep field polarization studies. This will be carried out in future work using hybrid deconvolution schemes such as A-projection Bhatnagar et al. (2013). Further a 3 percent squint in Stokes V and individual antenna pointing offsets, and instrumental polarization leakages need to be accounted for while imaging deep fields with the GMRT.

I have demonstrated the existence of alignments in the Radio AGN jets in the GMRT ELAIS N1 deep field as shown by the Kuiper and Watson U^2 statistics both demonstrate 99 % significance of deviation from uniformity, for the extracted and the redshift sub-sample of AGN jet position angles. By means of the variogram test of the position angles established position angle correlation at angular scales of 1.2°- 1.8 degrees°, corresponding to a comoving scale of 50-75h^{-1}Mpc at a redshift of one.

By means of the two-point correlation function , the Ripley's K function and the Lieshout - Baddeley J function the presence of spatial correlations in the observed galaxy distribution in the ELAIS N1 field at the scale of 5-24 minutes of arc in angular separation corresponding to 3-16 h^{-1}Mpc in comoving distance scale at a redshift of 1. This implies that the position angle alignment does not trace the spatial clustering and extends to larger scales.

6.0.11 Future Work

The ability to probe the alignments in radio galaxy jet positions angles at large scales such as $1000h^{-1}$Mpc requires wider (larger angular coverage) and deeper(faint flux levels) imaging. The incorporation of primary beam corrections to obtain a fully direction dependance corrected mosaic is of utmost importance to probe fainter flux levels(more sources). The need to account for the effects as a part of deconvolution has been identified and efforts have gone into integrating the algorithms into CASA. To be able to correct for the primary beam rotation and elongation a more accurate model of the aperture illumination function (Fourier transform of the primary beam) is required to achieve this more observing time has been allocated at the GMRT observatory.

Analysis of alignments as a function of redshift and cosmic volume can be studied better if complete redshift information was available which would also enable us directly verify earlier results of varying alignments strengths reported as a function of redshift by Hutsemékers and Lamy (2001). In the presence of complete redshift information that we hope to obtain from the SERVS catalogs a three dimensional correlation across angular scales can be identified.

The alignments of radio galaxy jets involves two populations, FRI and FRII. I hope to be able to identify if the alignments and the correlation scales are unique to either of the populations. This requires a larger sample requiring a larger area being probed. As a complement of the ELAIS N1 deep survey a wide area survey has been carried out to about a third of the current depth covering $2deg^2$, which is an ideal dataset for the extension of our current analysis. The dataset covers a large area this increases the number density of of the extended AGN jet sources which will improve our sample size and statistical analysis significantly. The large area covered allows us to probe the AGN jet alignments on much larger scales and verify the alignment results of Hutsemékers and Lamy (2001) and establish beyond reasonable doubt the effectiveness of using radio jet alignments as a probe of large scale alignments.

Bibliography

Baddeley, A. and Turner, R., 2005. Spatstat: an R package for analyzing spatial point patterns. *Journal of Statistical Software*, 12(6):1–42.

Banfield, J. K., George, S. J., Taylor, A. R., Stil, J. M., Kothes, R., and Scott, D., 2011. Polarized Radio Sources: A Study of Luminosity, Redshift, and Infrared Colors. *The Astrophysical Journal*, 733:69.

Battye, R. and Browne, I., 2009. Radio and optical orientations of galaxies. *Monthly Notices of the Royal Astronomical Society*, 399(4):1888–1900.

Bhatnagar, S., Cornwell, T. J., Golap, K., and Uson, J. M., 2008. Correcting direction-dependent gains in the deconvolution of radio interferometric images. *Astronomy & Astrophysics*, 487:419–429.

Bhatnagar, S., Rau, U., and Golap, K., 2013. Wide-field wide-band Interferometric Imaging: The WB A-Projection and Hybrid Algorithms. *The Astrophysical Journal*, 770:91.

Born, M. and Wolf, E., 1999. *Principles of Optics: Electromagnetic Theory of Propagation, Interference and Diffraction of Light*. Cambridge University Press.

Chengalur, J., Gupta, Y., and Dwarkanath, K. S., editors, 2003. *Low Frequency Radio Astronomy*. National Centre for Radioastrophysics.

Clark, B., 1980. An efficient implementation of the algorithm'clean'. *Astronomy and Astrophysics*, 89:377.

Condon, J. J., Cotton, W. D., Greisen, E. W., Yin, Q. F., Perley, R. A., Taylor, G. B., and Broderick, J. J., 1998. The NRAO VLA Sky Survey. *The Astronomical Journal*, 115:1693–1716.

Cornwell, T. J., Golap, K., and Bhatnagar, S., 2005. W Projection: A New Algorithm for Wide Field Imaging with Radio Synthesis Arrays. In Shopbell, P., Britton, M., and Ebert, R., editors, *Astronomical Data Analysis Software and Systems XIV*, volume 347 of *Astronomical Society of the Pacific Conference Series*, page 86.

Diggle, P. J. and Jr, P. J. R., 2007. *Model Based Geostatistics*. Springer, New York.

Feigelson, E. D. and Jogesh Babu, G., 2012. *Modern Statistical Methods for Astronomy*. Cambridge University Press.

Garn, T., Green, D. A., Riley, J. M., and Alexander, P., 2008. A 610-MHz survey of the ELAIS-N1 field with the Giant Metrewave Radio Telescope - observations, data analysis and source catalogue. *Monthly Notices of the Royal Astronomical Society*, 383:75–85.

Hamaker, J. P., Bregman, J. D., and Sault, R. J., 1996. Understanding radio polarimetry. I. Mathematical foundations. *Astronomy & Astrophysicss*, 117:137–147.

Hancock, P. J., Murphy, T., Gaensler, B. M., Hopkins, A., and Curran, J. R., 2012. Compact continuum source finding for next generation radio surveys. *Monthly Notices of the Royal Astronomical Society*, 422:1812–1824.

Hawley, D. L. and Peebles, P. J. E., 1975. Distribution of observed orientations of galaxies. *The Astronomical Journal*, 80:477–491.

Heckman, T. M. and Kauffmann, G., 2006. The host galaxies of AGN in the Sloan Digital Sky Survey. *New Astronomy Review*, 50:677–684.

Högbom, J., 1974. Aperture synthesis with a non-regular distribution of interferometer baselines. *Astron. Astrophys. Suppl*, 15(1974):417–426.

Hutsemékers, D., 1998. Evidence for very large-scale coherent orientations of quasar polarization vectors. *Astronomy & Astrophysics*, 332:410–428.

Hutsemékers, D. and Lamy, H., 2001. Confirmation of the existence of coherent orientations of quasar polarization vectors on cosmological scales. *Astronomy & Astrophysics*, 367:381–387.

Illian, J., Penttinen, A., Stoyan, H., and Stoyan, D., 2008. *Statistical analysis and modelling of spatial point patterns*, volume 70. John Wiley & Sons.

Jaeger, S., 2008. The Common Astronomy Software Application (CASA). In Argyle, R. W., Bunclark, P. S., and Lewis, J. R., editors, *Astronomical Data Analysis Software and Systems XVII*, volume 394 of *Astronomical Society of the Pacific Conference Series*, page 623.

Jammalamadaka, S. and Sengupta, A., 2001. *Topics in Circular Statistics*. Series on multivariate analysis. World Scientific.

Jansky, K. G., 1933. Radio Waves from Outside the Solar System. *Nature*, 132:66.

Jr, P. J. R. and Diggle, P. J., 2001. geoR: a package for geostatistical analysis. *R-NEWS*, 1(2):14–18.

Kim, J.-W., Edge, A. C., Wake, D. A., and Stott, J. P., 2011. Clustering properties of high-redshift red galaxies in SA22 from the UKIDSS Deep eXtragalactic Survey. *Monthly Notices of the Royal Astronomical Society*, 410:241–256.

Landy, S. D. and Szalay, A. S., 1993. Bias and variance of angular correlation functions. *The Astrophysical Journal*, 412:64–71.

Lawrence, A., 1987. Classification of active galaxies and the prospect of a unified phenomenology. *Publications of the Astronomical Society of the Pacific*, pages 309–334.

van Lieshout, M. N. M. and Baddeley, A. J., 1996. A nonparametric measure of spatial interaction in point patterns. *Statistica Neerlandica*, 50(3):344–361.

Martinez, V. J. and Saar, E., 2010. *Statistics of the galaxy distribution*. CRC Press.

Matthews, T. A. and Sandage, A. R., 1963. Optical Identification of 3c 48, 3c 196, and 3c 286 with Stellar Objects. *The Astrophysical Journal*, 138:30.

Neyman, J. and Scott, E. L., 1958. Statistical approach to problems of cosmology. *Journal of the Royal Statistical Society. Series B (Methodological)*, pages 1–43.

Offringa, A. R., 2010. AOFlagger RFI Software. Astrophysics Source Code Library.

Peebles, P. J. E., 1973. Statistical Analysis of Catalogs of Extragalactic Objects. I. Theory. *The Astrophysical Journal*, 185:413–440.

Ratra, B., 1992. Cosmological 'seed' magnetic field from inflation. *The Astrophysical Journall*, 391:L1–L4.

Rau, U., Bhatnagar, S., Voronkov, M. A., and Cornwell, T. J., 2009. Advances in Calibration and Imaging Techniques in Radio Interferometry. *IEEE Proceedings*, 97:1472–1481.

Rusk, R., 1990. Optical polarization properties of compact radio sources. *Journal of the Royal Astronomical Society of Canada*, 84:199–215.

Ryle, M., 1955. The application of interferometric methods in radio astronomy. *Vistas in Astronomy*, 1(0):532 – 541.

Sault, R. J., Hamaker, J. P., and Bregman, J. D., 1996. Understanding radio polarimetry. II. Instrumental calibration of an interferometer array. *Astronomy & Astrophysicss*, 117:149–159.

Seyfert, C. K., 1943. Nuclear Emission in Spiral Nebulae. *The Astrophysical Journal*, 97:28.

Sirothia, S. K., Dennefeld, M., Saikia, D. J., Dole, H., Ricquebourg, F., and Roland, J., 2009. 325-MHz observations of the ELAIS-N1 field using the Giant Metrewave Radio Telescope. *Monthly Notices of the Royal Astronomical Society*, 395:269–281.

Snec, R. D., 1974. Biometrika tables for statisticians, volume 2. *Technometrics*, 16(3):480–481.

Stockman, H. S., Angel, J. R. P., and Miley, G. K., 1979. Alignment of the optical polarization with the radio structure of QSOs. *The Astrophysical Journall*, 227:L55–L58.

Taylor, A. R., Stil, J. M., Grant, J. K., Landecker, T. L., Kothes, R., Reid, R. I., Gray, A. D., Scott, D., Martin, P. G., Boothroyd, A. I., Joncas, G., Lockman, F. J., English, J., Sajina, A., and Bond, J. R., 2007. Radio polarimetry of the elais n1 field: Polarized compact sources. *The Astrophysical Journal*, 666(1):201.

Taylor, G. B., Carilli, C. L., and Perley, R. A., editors, 1999. *Synthesis Imaging in Radio Astronomy II*, volume 180 of *Astronomical Society of the Pacific Conference Series*.

Torres, D. F. and Anchordoqui, L. A., 2004. Astrophysical origins of ultrahigh energy cosmic rays. *Reports on Progress in Physics*, 67:1663–1730.

Totsuji, H. and Kihara, T., 1969. The Correlation Function for the Distribution of Galaxies. *Publications of the Astronomical Society of Japan*, 21:221.

Wall, J. V. and Jenkins, C. R., 2012. *Practical statistics for astronomers*. Cambridge University Press.